Analytical Investigation of Active Control of Radiated Inlet Noise from Turbofan Engines

by

John D. Risi
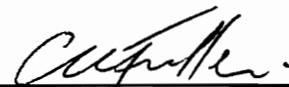
Thesis submitted to the Faculty of
Virginia Polytechnic Institute and State University
in partial fulfillment of the requirements for the degree of
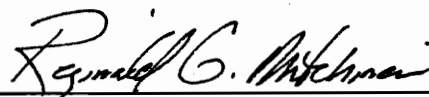
Master of Science
in
Mechanical Engineering

APPROVED:

_____
Dr. Ricardo A. Burdisso, Chairman

_____
Dr. Chris R. Fuller

_____
Dr. Reginald G. Mitchiner

May, 1995
Blacksburg, Virginia

C.2

ANALYTICAL INVESTIGATION OF ACTIVE CONTROL OF RADIATED INLET NOISE FROM TURBOFAN ENGINES

by

John D. Risi

Committee Chairman: Ricardo A. Burdisso

Mechanical Engineering Department

ABSTRACT

An analytical model has been developed to study the potential of active noise control techniques for reducing radiated tonal inlet noise from turbofan engines. The analytical model consists of multiple control sources placed in the periphery of the engine inlet duct which inject anti-noise into the duct to destructively interfere with the sound field generated by the fan. The development of the analytical expressions of the radiated sound fields due to both the fan disturbance and the control sources is based on duct modal expansion. Numerical analyses are presented for different system configurations of secondary control sources and error sensors. Two error sensing strategies are considered in this work. The first approach uses microphones placed in the acoustic far field. The second sensing technique consists of placing distributed error sensors in the engine inlet. Attenuation of the radiated sound field is accomplished using a multi-channel feedforward control approach. Control signals are calculated to minimize the pressure disturbance at desired error sensor locations and are then used to determine the controlled radiated sound field. The performance of selected system configurations are

discussed and the sensitivity to system parameter variation to the control of inlet noise is explored. Reductions in the radiated sound power level of 4 to nearly 28 dB is demonstrated. It is also demonstrated that for global attenuation of the far field pressure multiple axial arrays of control sources are required. The model can be used to evaluate performance envelopes for various system configurations including sensitivities to error sensor and control source locations, control channel configurations and the effects of mean flow within the inlet duct. The model can also be extended for use in design optimization.

Acknowledgements

Table of Contents

List of Figures

List of Tables

Chapter 1

Introduction

Noise is a significant negative factor associated with the modern commercial airline industry. When turbojets were first introduced, the primary source of noise was from the engine exhaust in the take-off configuration. The high power settings required for climb-out created a broad-band exhaust noise that dominated in the vicinity of the take-off path of the aircraft. During approach, when the engine is at or near idle condition, the discrete high frequency whine of the compressors becomes dominant [1]. As engines evolved from turbojet to primarily turbofan cycles, fan noise has become an increasingly larger contributor of total engine noise. The impending use of ultra high bypass ratio engines will result in an even greater fan noise component at lower frequencies. Commercial noise reduction techniques to date consist primarily of passive liners. For engine exhaust noise, the application of duct liners has proven adequate in reducing the wide-band noise field. The length of the exhaust duct of a turbojet engine is often sufficient to accommodate the required duct lining material. Also, in the exhaust stream, the engine duct modes propagate away from the engine axis and toward the duct periphery, increasing the attenuation effect of the duct liners. At the turbofan inlet, however, the duct modes propagate against the boundary layer and are refracted toward the engine axis making the duct liners less effective. In addition, the shorter and larger

1

diameter inlet ducts inherent to the ultra high bypass engines and the lower blade passage frequencies expected for these engines will make passive attenuation of the inlet fan noise even more difficult. In order to meet forecast noise level requirements, active noise control techniques may have the potential to overcome these problems.

The concept of active sound control, or anti-noise as it is sometimes referred, is attributed to Paul Leug [2]. Active noise control works on the principle of destructive interference between sound fields generated by the original primary source and that due to an array of secondary sources, whose acoustic outputs can be controlled. For example, if the amplitude and phase of a signal driving one sound source are adjusted relative to that driving another source, the acoustic pressure at any single point in the resulting sound field can be driven to zero. Unfortunately, it is also possible that at other points in the sound field the two components of pressure will be in-phase and constructive interference will occur, increasing the sound level at these points. One of the principle tasks of active noise control is then the generation and control of an operating signal of the secondary source in order to globally reduce the acoustic field of interest.

The potential of the active noise control of turbomachines has been demonstrated experimentally at Virginia Tech [3-5]. In this work, the tonal noise radiated by the fan from a Pratt and Whitney JT15D turbofan engine was controlled using an adaptive feedforward control algorithm. The control source transducers were electromagnetic loudspeakers attached to the engine inlet duct while error microphones, placed in the

acoustic far field, monitored the resultant sound field. The experimental team successfully demonstrated reduction of the radiated sound from the engine at the fan blade passage frequency within a zone in front of the engine. This zone extended approximately 30° on either side of the engine centerline axis with attenuation levels reaching 16 dB. However, at angles greater than ±30°, toward the sideline regions, the sound power levels increased above the level of the uncontrolled fan noise. The team also demonstrated the simultaneous control of multiple tones radiated from the engine. In an attempt to control the blade passage frequency tone and the first harmonic, attenuation in localized areas of as much as 12 dB was achieved. Likewise, attenuation levels of 7 dB to 16 dB was achieved using a multiple channel control system to control the fan blade passage tone and the high-pressure compressor blade frequency tone. The control of multiple tones appeared to create less sideline spillover as well.

The results from this experimental work sparked analytical efforts in this area. Kraft and Kontos [6] developed a model to explore the theoretical implications of active control of turbofan engine noise. The secondary control source of their model is a single axial station comprised of electromagnetic sources located in the engine duct, flush with the outer wall of the inlet duct, coupled to the duct by a short horn. The authors assume a single mode to be present in the inlet duct. They develop the theory required to determine the optimum number of active noise control sources needed to obtain global control of the sound field radiated from the engine due to a single mode. The efficiency of conversion of electrical energy into acoustical energy for electromagnetic loudspeakers

3

radiating into the duct was also addressed.

Berge et al. [7] used the boundary element method to evaluate the concept of active noise control for turbofan noise reduction. Their prime objective was not to reduce the acoustical field in all directions, but to reduce only certain regions of the far field radiation which are of concern, such as the aircraft cabin or the flyover area of the aircraft. They accept the consequence that an increase in sound pressure levels may occur and attempt to direct this higher sound energy to convenient domains.

Fleeter [8] investigated the potential of active noise control by placing control sources at the stator vanes rather than in the inlet wall. The model was comprised of an upstream fan stage and a downstream fan exit guide vane. To cancel the modes generated by the interaction of the fan rotor and guide vane, oscillating trailing edge flaps and oscillating pistons are assumed mounted on the stator vanes. Fleeter developed an analytical model to demonstrate that complete cancellation of the propagating noise field is possible.

In this work, an analytical model is developed to predict the radiated acoustic field at a single frequency from both the engine inlet and an active noise control system. The engine inlet noise field is assumed composed of a known set of spinning modes. The control sources are modeled as point sources located on the periphery of the engine inlet duct. Two sensing strategies are considered in this study. The first approach uses microphones placed in the acoustic far field which monitor the variable of interest, i.e. far field pressure. The second sensing technique consists of placing the error sensors in

4

the same engine inlet. In this case, the error transducers do not directly measure the far field pressure. The optimum control inputs to the secondary sources are obtained by minimizing the sum of the error signal mean-square-values. These control inputs are then applied to the secondary sources to compute the controlled acoustic field.

The main objectives of this work are to analytically explore the potential of active noise control techniques in attenuating inlet noise and to uncover the mechanisms of control. A model is desired that has the capability of investigating the selection of physical control system parameters in order to lend some assistance to the design of experimental apparatuses. An analytical model can also be used to determine the effects of parameter variation on the ability of the control system to attenuate the fan noise. Finally, a model of the active control system can be used to determine if error sensors mounted in the inlet of the engine can be effective in the attenuation of far field noise.

To achieve these objectives, a model has been developed that is simple, yet it contains the main aspects of active noise control. The model is realistic in its structure. Error sensors and secondary control sources are modeled to simulate actual physical components. The complex control inputs required to drive the secondary control sources are calculated in a manner similar to that used in experimental conditions. A more complex model is not required at this time. For example, an aerodynamic model for the turbomachine source mechanism would make it more difficult to understand the basic control mechanisms.

5

1.1 Thesis Organization

Chapter 2 presents the development of the analytical models of the acoustic field inside the inlet and in the far field for the fan and point control sources. Also included in Chapter 2 are the details of the structure and operation of the feedforward control algorithm used in the simulation of the active noise control study. In Chapter 3 the analytical model is tested and its operation is verified through a comparison to experimental results obtained from the researchers at Virginia Tech [3-5]. Numerical results are then presented for far field error transducers and for distributed error sensors mounted within the inlet duct itself. A parametric investigation was conducted using the model to determine the optimal system configurations, including the ideal locations of the secondary control sources and error transducers. The development of this parametric investigation is outlined and results for the two different sensing strategies are presented. Chapter 3 also includes the results of a sensitivity study for the analytical model of the active control system. Here various parameters are modified for single and multiple axial control source arrays, for both far field and inlet error sensors, in an attempt to determine the advantages and limitations of more complex control structures. Initial investigation into the effects of modified control system parameters is conducted and modal breakdowns of sample case studies are presented. Also in Chapter 3, the analytical model is extended to include the effect of mean flow present in the inlet duct and the work completed to date is then compared to research conducted by an outside

researcher using a principle component analysis approach to study the active control of the radiated tonal inlet noise. Finally, some conclusions to the work contained within are drawn and recommendations for future and more advanced work are offered in Chapter 4.

Chapter 2

2. Mathematical Model

The analytical effort undertaken involves the mathematical modeling of the radiated sound field due to both the engine fan and the secondary control sources, and the simulation of the feedforward control algorithm. Figure 2.1 shows a schematic of a feedforward active control system implemented in a turbofan engine duct. The secondary control sources are placed on the periphery of the inlet duct while the error sensors are positioned in the acoustic far field. It is noted here that only the case of far field error sensors is shown. Use of error transducers placed in the inlet duct is also investigated in this work and will be discussed in detail later. The rotating fan blades pictured in Figure 2.1 produce a disturbance sound field at the blade passage frequency (BPF) and its harmonics. This undesired noise field propagates down the engine inlet and radiates into the far field. A proximity sensor mounted on the engine, at or near the fan station, generates sinusoidal signals at the BPF and harmonics which are input into an array of compensators. The outputs from the compensators are the control signals. The array of secondary sources, driven by the control signals, generates the secondary sound field that destructively interferes with the disturbance noise field. The optimum control inputs are determined to minimize the pressure at the array of error sensors placed in the acoustic far field or installed within the inlet duct itself. In this chapter,
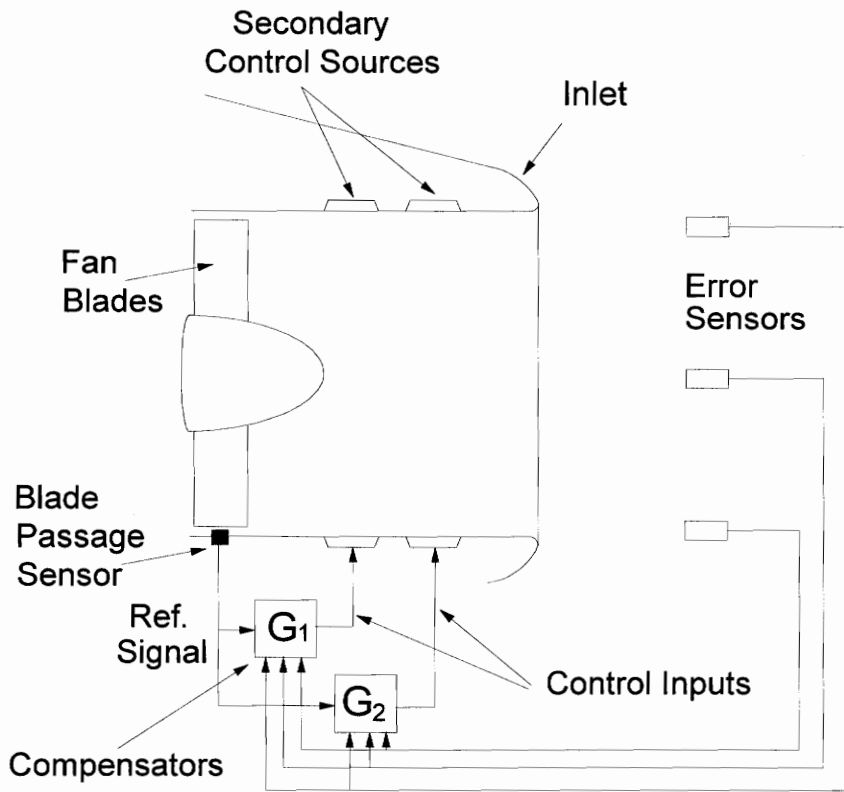
Figure 2.1. Schematic of a feedforward active control system.

the analytical expressions are developed which describe the fan disturbance noise field, the control source noise field and the feedforward control algorithm.

2.1 Fan Disturbance Noise Field

The aerodynamic noise generation mechanisms in turbomachinery is a subject of intensive research on its own and is beyond the scope of this work. Tyler and Sofrin [9] were some of the first to investigate the source and characteristics of noise generated by aircraft in their paper on axial compressor noise in 1962. They showed that the sound radiation from a turbojet engine depends crucially on the presence of spinning mode patterns. The sources of the dominant noise in a turbojet engine are due to the effects of steady aerodynamic rotor blade loading. The pressure pattern associated with the spinning of the rotor spins with rotor angular velocity $\omega = 2\pi N$, where N is the rotor shaft speed. If there are B blades in the rotor spaced $2\pi/B$ radians apart, then the associated pressure contours repeat in this interval. The rotor pressure field then consists of a superposition of lobed patterns all turning with rotor speed N. The fundamental blade passage frequency, BN, is associated with a B-lobe pattern and the harmonics 2BN and 3BN are associated with patterns having 2B and 3B lobes. The authors also describe other aspects of the compressor noise problem including the duct transmission problem and the manner in which the noise field radiates to the free space. They present a quantitative method to determine the presence of a dominant propagating mode through

knowledge of the engine design.

To simplify the representation of the turbomachinery source for this work, the fan is assumed to produce a known set of spinning acoustic modes at the fan blade passage frequency (BPF). An acoustic mode is defined by the circumferential order m, and the radial order μ, written as (m,μ). Thus, the acoustic mode of order (0,0) describes the plane wave mode. The pressure due to the fan disturbance noise is assumed to be specified on a reference plane normal to the engine axis at x=0. Then, the pressure distribution throughout the circular inlet duct is determined so that the radiation from the inlet opening can be evaluated.

The cylindrical coordinate system (r,θ,x) used in the analysis is shown in Figure 2.2. The disturbance pressure field in a cylindrical duct of radius a at the BPF can be expressed as the contribution of spinning modes or characteristic functions traveling in the positive x-direction [9,10]. Without lost of generality, only modes rotating in the positive θ-direction are considered here. Thus,

$$(P_i)_d(r,\theta,x,t) = \sum_{m,\mu} A_{m\mu} \, J_m(k_{m\mu}r) \; e^{-im\theta} e^{-ik_x x} e^{i\omega t} \tag{2.1}$$

where $A_{m\mu}$ is the known complex amplitude of the (m,μ) spinning mode pattern, J_m is the mth order Bessel function and k_x is the axial wave number given by
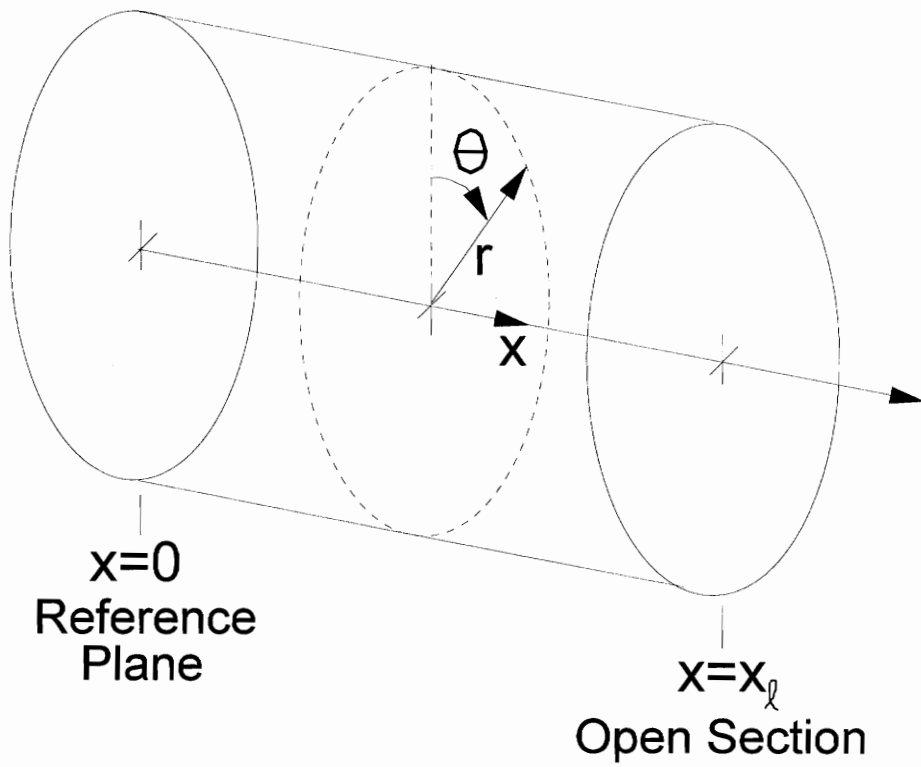
Figure 2.2. Cylindrical coordinate system for inlet duct analysis.

$$k_x = \sqrt{\left(\frac{\omega}{c}\right)^2 - k_{m\mu}^2} \qquad (2.2)$$

where $\omega = \omega_r B$, ω_r is the fan rotating angular velocity, B is the number of fan blades and c the speed of sound in air. The modal wave number or eigenvalue $k_{m\mu}$ is determined by the system radial boundary conditions. Here, the rigid wall condition for the inlet duct implies that the radial component of the fluid particle velocity at $r=a$ must vanish. This leads $k_{m\mu}$ to be defined as

$$k_{m\mu} = \frac{j'_{m\mu}}{a} \qquad (2.3)$$

where $j'_{m\mu}$ are the inflection points of J_m at $(dJ_m/dx) = 0$ [10]. The propagation characteristic of the modes is determined by the axial wavenumber k_x. A mode will propagate for $k_{m\mu} < \omega/c$ and it will be attenuated when $k_{m\mu} > \omega/c$. The frequency at which this change occurs is called the cut-off frequency. Only the propagating modes are included in the expression of Eq.(2.1). Setting the circumferential order m to zero in Eq.(2.1) leads to the special case of the axisymmetric modes, i.e. plane wave and higher order radial modes. In the sequel, the time dependent term $e^{i\omega t}$ will be omitted for simplicity.

13

2.2 Point Source Sound Field

The noise radiated by the fan is actively reduced by an array of N_s control sources mounted in the engine inlet. The sound field generated by the control sources will destructively interfere with the fan noise thus reducing the inlet radiated far field noise. The control sound source is modeled as an array of point sources distributed on the duct wall. Thus, an expression for the acoustic field produced by a simple source located at the duct wall is required. This is approximated using the Green's function on a hard walled semi-infinite duct. Assuming the nth point source is located at (a, θ_n, x_n) as presented in Figure 2.1, the Green's function for a positive-x traveling wave can be written as [11]

$$(P_i)_c^n(r,\theta,x) = \frac{-i}{2\pi a^2} \sum_{m,\mu} \frac{\Psi_{m\mu}(r,\theta)\Psi_{m\mu}(a,\theta_n)}{\Lambda_{m\mu} k_x} e^{-ik_x|x_t - x_n|} \tag{2.4}$$

where the duct acoustic mode shape, $\Psi_{m\mu}$, is defined as

$$\Psi_{m\mu}(r,\theta) = \cos(m(\theta - \theta_n)) J_m(k_{m\mu}r) \tag{2.5}$$

and $\Lambda_{m\mu}$ is the mean-square amplitude of the cross-duct mode defined as

$$\Lambda_{m\mu} = \frac{1}{\varepsilon_m} \left[1 - \frac{m^2}{(k_{m\mu}a)^2} \right] J_m^2(k_{m\mu}a) \tag{2.6}$$

where $\varepsilon_m = 1$ for $m = 0$ and $\varepsilon_m = 2$ for $m > 0$.

14

2.3 Radiated Far Field Pressure

The sound field generated by both the fan and the control sources propagates along the duct to the open end at $x=x_\ell$ where it then radiates into the far field. The spherical coordinate system (R,β,Φ) used to compute the pressure radiated to the far field is shown in Figure 2.3. The non-uniform pressure distribution at the duct opening can be determined using the expressions of Eqs.(2.1) and (2.4). To compute the sound radiated into the far field, the velocity fluctuation across the duct opening is assumed to be volume velocity sources [12]. Further assuming the inlet of the duct to be embedded in a baffle, the pressure radiated at a point in the far field defined by (R,β,Φ) is obtained by using the Rayleigh integral as [13]

$$P_{\!f\!f}(R,\beta,\Phi) = \frac{i\omega\rho}{2\pi}\int_S v_x(r,\theta)\,\frac{e^{-ik_o h}}{h}\,dS \qquad (2.7)$$

where, referring to Figure 2.3, R is the position vector of the observation point, r is the position vector of the elemental surface dS having normal velocity $\upsilon_x(r,\theta)$ and h is the magnitude of the vector R-r. The elemental surface dS can be written in terms of r and θ as $dS=rdrd\theta$. Also, ρ is the density of air and $k_o=\omega/c$ is the acoustic wave number. Eq.(2.7) assumes that the reflection from the duct opening is negligible. This is a reasonable approximation except near the cut-on frequency of the modes [12].

The fluid particle velocity normal to the duct opening, $v_x(r,\theta)$, in Eq.(2.7) is computed as

15
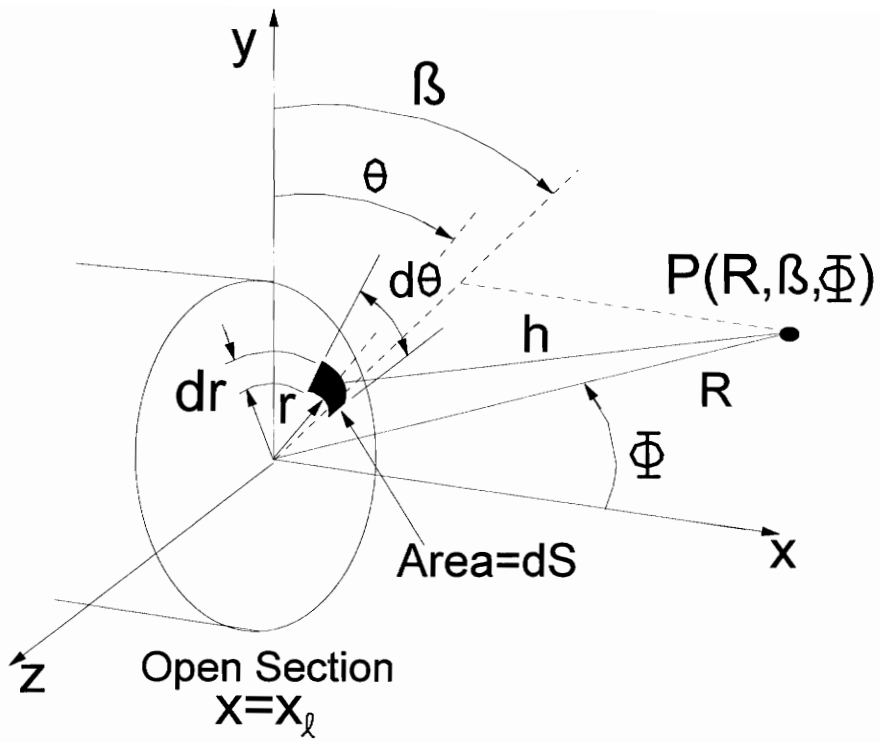
Figure 2.3. Spherical coordinate system showing spatial relation to acoustic far field and details of open section.

$$v_x(r,\theta) = -\frac{1}{i\omega\rho}\frac{\partial P}{\partial x}\bigg|_{x=x_t} \tag{2.8}$$

From Figure 2.3, an expression for the magnitude of the vector R-r can be obtained as

$$\vec{h} = \vec{R} - \vec{r} \tag{2.9}$$

where

$$\vec{R} = R\cos(\Phi)\,\hat{i} + R\sin\Phi\,\sin\beta\,\hat{j} + R\sin\Phi\,\cos\beta\,\hat{k} \tag{2.10}$$

$$\vec{r} = r\sin\theta\,\hat{j} + r\cos\theta\,\hat{k} \tag{2.11}$$

Substituting Eqs.(2.10) and (2.11) into Eq.(2.9) and combing like terms yields

$$\vec{h} = R\cos\Phi\,\hat{i} + (R\sin\Phi\sin\beta - r\sin\theta)\,\hat{j} + (R\sin\Phi\cos\beta - r\cos\theta)\,\hat{k} \tag{2.12}$$

Taking the magnitude of the vector on both sides of Eq.(2.12) and simplifying, the magnitude of the vector h can be written as

$$h^2 = R^2\left(1 + \frac{r^2}{R^2} - \frac{2r}{R}\sin\Phi\cos(\theta-\beta)\right) \tag{2.13}$$

Assuming the far field approximation $R >> r$, the term r^2/R^2 can be neglected. Then, Eq.(2.13) can be written as

17

$$h = R \left(1 - \frac{2r}{R} \sin\Phi \cos(\theta - \beta)\right)^{\frac{1}{2}} \tag{2.14}$$

Using the expansion series

$$(1 - x)^{\frac{1}{2}} = 1 - \frac{1}{2} x - \frac{1}{8} x^2 - \dots \tag{2.15}$$

and eliminating higher order terms, Eq.(2.14) becomes

$$h \simeq R - r \sin\Phi \cos(\theta - \beta) \tag{2.16}$$

Replacing Eq.(2.16) into the Rayleigh integral gives

$$P_{ff}(R,\beta,\Phi) = \frac{i\omega\rho}{2\pi} \frac{e^{-ik_oR}}{R} \int_S v_x(r,\theta) e^{ik_o r \sin\Phi \cos(\theta - \beta)} dS \tag{2.17}$$

where it has been further assumed that h=R in the denominator of Eq.(2.17). The acoustic far field pressure due to the fan disturbance and the control point source can now be computed.

2.3.1   Fan Disturbance

The far field pressure due to the fan disturbance is obtained by substituting Eq.(2.1) into (2.8) and this into the Rayleigh integral of Eq.(2.17). Thus, the pressure at (R,β,Φ) in the far field due to fan noise is given as

$$(P_{ff})_d = \sum_{m,\mu} \frac{iA_{m\mu}k_x}{2\pi R} e^{-i(k_x x_t + k_o R)} \int_S J_m(k_{m\mu}r) e^{-im\theta} e^{ik_o r \ \sin\Phi \ \cos(\theta-\beta)} dS \qquad (2.18)$$

Eq.(2.18) can be rewritten by referring to Figure 2.3 as

$$(P_{ff})_d = \sum_{m,\mu} \frac{iA_{m\mu}k_x}{2\pi R} e^{-i(k_x x_t + k_o R)} \int_0^{2\pi}\int_0^a J_m(k_{m\mu}r) e^{-im\theta} e^{ik_o r \ \sin\Phi \ \cos(\theta-\beta)} r \ drd\theta \qquad (2.19)$$

Breaking and expanding the double integral of Eq.(2.19), the integral in terms of θ can be expressed as

$$I_\theta = \int_0^{2\pi} [\cos(m\theta) - i \ \sin(m\theta)] \ e^{ik_o r \sin\Phi \ \cos(\theta-\beta)} d\theta \qquad (2.20)$$

The exponential term of Eq.(2.20) can be expanded in terms of Bessel functions as [14]

$$e^{ik_o r \ \sin\Phi\cos(\theta-\beta)} = J_0(k_o r\sin\Phi) + 2i^m J_m(k_o r\sin\Phi) \ \cos(m(\theta-\beta)) \qquad (2.21)$$

Substituting the expansion of Eq.(2.21) into Eq.(2.20) and rewriting with the terms that do not vanish at both of the limits of integration gives

$$I_\theta = 2i^m J_m(k_o r\sin\Phi)\left\{ \int_0^{2\pi}\cos(m(\theta-\beta))\cos(m\theta) \ d\theta \ - i\int_0^{2\pi}\cos(m(\theta-\beta))\sin(m\theta) \ d\theta \right\} \quad (2.22)$$

Applying trigonometric identities to Eq.(2.22) and completing the integration, the integral

19

in terms of θ of Eq.(2.20) becomes

$$I_\theta = 2\pi i^m J_m(k_o r\sin\Phi)[\cos(m\beta) - i\sin(m\beta)] \qquad (2.23)$$

or simplified to exponential form,

$$I_\theta = 2\pi i^m J_m(k_o r\sin\Phi) e^{-im\beta} \qquad (2.24)$$

Substituting Eq.(2.24) into Eq.(2.19) yields

$$(P_{ff})_d = \sum_{m,\mu} \frac{i^{m+1} k_x}{R} A_{m\mu} e^{-i(k_x x_t + k_o R + m\beta)} \int_0^a J_m(k_{m\mu} r) J_m(k_o r\sin\Phi) \ r \ dr \qquad (2.25)$$

The integral of Eq.(2.25) is now in terms of r only. Since this integral is the product of two Bessel functions, the integral in terms of r in Eq.(2.25) has a closed form solution [14]. Therefore, the pressure radiated to the far field due to fan noise can be written as

$$(P_{ff})_d(R,\beta,\Phi) = \sum_{m,\mu} i^{m+1} \frac{k_x A_{m\mu}}{R} e^{-i(k_x x_t + k_o R)} e^{-im\beta} I_r \qquad (2.26)$$

where I_r is defined as

$$I_r = \frac{a}{(k_{m\mu})^2 - (k_o\sin\Phi)^2} \left\{ k_{m\mu} J_m(k_o a \sin\Phi) J_{m+1}(k_{m\mu} a) - k_o\sin\Phi J_m(k_{m\mu} a) J_{m+1}(k_o a \sin\Phi) \right\} \qquad (2.27)$$

for $(k_{m\mu})^2 \neq (k_o\sin\Phi)^2$ and as

20

$$I_r = \frac{a^2}{2} \left\{ J_m^2(k_{m\mu}a) - \frac{2m}{k_{m\mu}a} J_m(k_{m\mu}a) J_{m+1}(k_{m\mu}a) + J_{m+1}^2(k_{m\mu}a) \right\} \qquad (2.28)$$

for $(k_{m\mu})^2 = (k_o \sin\Phi)^2$.

2.3.2   Point Source

The far field sound pressure due to a single source located within the duct is computed by replacing Eq.(2.4) into Eq.(2.8) and this into the Rayleigh integral of Eq.(2.17). Thus, the far field pressure due to a point source within the duct is written as

$$(P_{ff})_c^n = \sum_{m\mu} \frac{\Psi_{m\mu}(a,\theta_n)}{4\pi^2 a^2 R \Lambda_{m\mu}} e^{-i(k_x|x_t - x_n| + k_o R)} \int_S \Psi_{m\mu}(r,\theta) \ e^{ik_o r \ \sin\Phi \ \cos(\theta - \beta)} dS \qquad (2.29)$$

Eq.(2.29) can be rewritten by referring to Figure 2.3 as

$$(P_{ff})_c^n = \sum_{m\mu} \frac{\Psi_{m\mu}(a,\theta_n)}{4\pi^2 a^2 R \Lambda_{m\mu}} e^{-i(k_x|x_t - x_n| + k_o R)} \int_0^{2\pi}\int_0^a \Psi_{m\mu}(r,\theta) \ e^{ik_o r \ \sin\Phi \ \cos(\theta - \beta)} r \ dr d\theta \qquad (2.30)$$

Recalling the definition of the acoustic mode shape of Eq.(2.5), the double integral of Eq.(2.30) can be written as

$$I_{r,\theta} = \int_0^{2\pi}\int_0^a \cos(m(\theta - \theta_n)) \ J_m(k_{m\mu}r) \ e^{ik_o r \ \sin\Phi \cos(\theta - \beta)} r \ dr d\theta \qquad (2.31)$$

Separating the double integral of Eq.(2.31), the integral in terms of θ becomes

$$I_\theta = \int_0^{2\pi} \cos(m(\theta - \theta_n)) \ e^{ik_o r \ \sin\Phi \ \cos(\theta - \beta)} d\theta \qquad (2.32)$$

Applying trigonometric identities to the cosine term of Eq.(2.32), the integral can be written as

$$I_\theta = \int_0^{2\pi} [\cos(m\theta_n) \ \cos(m\theta) \ + \sin(m\theta_n) \ \sin(m\theta)] \ e^{ik_o r \ \sin\Phi \ \cos(\theta - \beta)} d\theta \qquad (2.33)$$

The terms within the integral of Eq.(2.33) are analogous to those in Eq.(2.20). Therefore, using similar operations applied to the fan noise, the integral in terms of θ for the control source noise becomes

$$I_\theta = 2\pi i^m \ J_m(k_o r \ \sin\Phi) \ \cos(m(\theta_n - \beta)) \qquad (2.34)$$

Substituting Eq.(2.34) into Eq.(2.31) and this into Eq.(2.30), the pressure in the far field due to a point source located within the duct becomes

$$(P_{ff})_c^n = \sum_{m\mu} \frac{i^m}{2\pi a^2 R \Lambda_{m\mu}} J_m(k_{m\mu} a) \ e^{-i(k_x|x_f - x_n| + k_o R)} \cos(m(\theta_n - \beta)) \int_0^a J_m(k_{m\mu} r) \ J_m(k_o r \ \sin\Phi) \ r \ dr \qquad (2.35)$$

The integral in Eq.(2.35) is now in terms of r only and is exactly the form of the integral of Eq.(2.25). Therefore, the solution of the integral in terms of r of Eq.(2.35) is Eq.(2.27) for $(k_{m\mu})^2 \neq (k_o \sin\Phi)^2$ and Eq.(2.28) for $(k_{m\mu})^2 = (k_o \sin\Phi)^2$. Completing the integration and simplifying, the pressure at a point (R, β, Φ) in the far field due to a point

22

source within the duct is [14]

$$(P_{ff})_c^n = \sum_{m\mu} \frac{i^m\, J_m(k_{m\mu}a)}{2\pi a^2 R\Lambda_{m\mu}}\ \cos(m(\theta_n - \beta))\ e^{-i(k_x|x_t - x_n| + k_r R)}\ I_r \tag{2.36}$$

where I_r is defined in Eqs.(2.27) and (2.28).

2.3.2.1   Array of Point Sources

Equations (2.4) and (2.36) define the pressure distribution in the inlet and in the far field, respectively, due to a single control source. In many practical systems, an array of secondary sources will be grouped in a single control channel. Thus, the inlet pressure due to the point sources grouped into the ℓth control channel can be written as

$$(P_i)_\ell = \{R_\ell\}^T \{(P_i)_c\} \tag{2.37}$$

and for the far field as

$$(P_{ff})_\ell = \{R_\ell\}^T \{(P_{ff})_c\} \tag{2.38}$$

where $\{(P_i)_c\}^T = \{(P_i)_c^1,\ldots,(P_i)_c^{Ns}\}$ and $\{(P_{ff})_c\}^T = \{(P_{ff})_c^1,\ldots,(P_{ff})_c^{Ns}\}$ are the vectors of inlet and far field pressure, respectively, due to each point source computed from Eqs. (2.4) and (2.36); $\{R_\ell\}$ is the control source configuration vector for channel ℓ; and the superscript T denotes the transpose. The elements in $\{R_\ell\}$ represent the magnitude and phase relative to each point source grouped into channel ℓ and driven by the ℓth control amplitude U_ℓ. The coefficients of $\{R_\ell\}$ are complex numbers so that any relative magnitude and phase between the sources can be defined. However, in this initial work

23

the elements of $\{R_\ell\}$ will take the form of 1, -1 and 0 representing in-phase, out-of-phase, or disconnected condition, respectively.

The total far field pressure due to the N_c control channels can then be expressed as

$$(P_i)_{cs} = \{U\}^T [R]\{(P_{ff})_c\} \; ; \; (P_{ff})_{cs} = \{U\}^T [R]\{(P_{ff})_c\} \qquad \text{(2.39 a, b)}$$

where $\{U\}^T = \{U_1, \ldots, U_{Nc}\}$ is the vector of N_c complex control amplitudes and the matrix [R] is the control configuration matrix for the N_c control channels. The ℓth row of this matrix is the vector $\{R_\ell\}$ previously described.

The total acoustic field is computed by using the expressions in Eqs.(2.1), (2.26) and (2.39) for both the fan and control fields. The total sound pressure at a point in the inlet is defined as

$$(P_i)_t = (P_i)_d + (P_i)_{cs} \qquad \text{(2.40)}$$

and in the far field as

$$(P_{ff})_t = (P_{ff})_d + (P_{ff})_{cs} \qquad \text{(2.41)}$$

2.4 Active Control Algorithm

A feedforward technique is selected as the control approach. In a feedforward approach, the control inputs are obtained such that some responses of the system are minimized. The response variables to be minimized are monitored with transducers referred to as

error sensors. In the system investigated here, for example, the error sensors would be acoustic pressure transducers, i.e. microphones.

For any feedforward control system, the error outputs can be written as the superposition of the primary or disturbance response and the secondary or control response. That is, the response at the eth error sensor is given as

$$y_t^e = y_d^e + \{y_c^e\}^T \{U\} \tag{2.42}$$

where y_t^e is the total response; y_d^e is the response due to the disturbance source; $\{y_c^e\}$ is the vector of error responses due to each control input; and $\{U\}$ is the vector of N_C control inputs. In a practical system an array of N_E error sensors are placed at critical locations in the system. Thus, Eq.(2.42) can be rewritten in matrix form as

$$\{y_t^e\} = \{y_d^e\} + [T] \{U\} \tag{2.43}$$

where now $\{y_d^e\}$ is the vector of error responses due to the primary disturbance and the (e, ℓ) elements of matrix $[T]$ represent the complex output at the eth sensor due to a unit input of the ℓth control channel.

In feedforward control, the optimum complex control inputs, U_ℓ, are obtained by minimizing a cost function. This cost function is commonly defined as the sum of the error output mean-square-value. Then,

$$C(U_\ell) = \{y_t^e\}^T \{y_t^e\}^* \tag{2.44}$$

It is easy to show that the optimum control inputs are the solution of the following linear

25

system of equations.

$$\{y_d^e\} + [T]\{U\} = 0 \qquad (2.45)$$

If the number of error sensors is greater than the number of control channels, $N_E > N_C$, the system is under-determined. A pseudo-inverse technique [15] can be used to solve for $\{U\}$ as

$$\{U\} = -([T]^T [T])^{-1} [T]^T \{y_d^e\} \qquad (2.46)$$

For the case of equal number of control channels and error sensors, $N_C = N_E$, Eq.(2.46) reduces to

$$\{U\} = -[T]^{-1} \{y_d^e\} \qquad (2.47)$$

if the matrix [T] is not rank deficient.

2.4.1   Error Transducers

The analytical investigation into the control mechanisms of active control of radiated tonal inlet noise from turbofan engines uses two different error sensing strategies. First, point microphones are assumed placed in the acoustic far field in front of the inlet duct to measure the resulting radiation, as shown earlier in Figure 2.1. In an approach to model what is expected to be a more physically feasible implementation, distributed error transducer films are assumed placed in the inlet duct periphery, upstream of the array(s) of secondary control sources. A schematic of the inlet duct and

control algorithm using inlet mounted error sensors is presented in Figure 2.4.

The use of far field microphones as error sensors is certainly not feasible in actual flight. However, they are considered in this study for two reasons. First, since they directly observe the quantity to be minimized, i.e. far field radiated pressure, the results can be used as a reference or upper limit performance bound. The performance of realistic sensing strategies can then be compared against this "optimal" far-field sensing strategy. Secondly, although no physical transducer can be placed in the far field, the far field pressure can be estimated using transducers placed at other locations, i.e. on the fuselage or inside the inlet. Transfer functions between these physically possible transducers and the far field pressure can be analytically or experimentally modeled. The output of the error transducers are then input into these transfer functions to predict the far field pressure. In addition, the use of error sensors mounted in the acoustic far field from a turbofan source is practical when considering the case of a stationary turbofan source such as a laboratory test site or runway engine run-up area at an airport.

2.4.1.1   Far Field Error Sensors

For the development of the control simulation for the case of far field error sensors, an array of N_E microphone error sensors ($N_E \geq N_C$) is assumed placed in the far field to monitor the resultant acoustic field. Each error microphone is defined by the coordinates (R_e, β_e, Φ_e). The optimum complex control amplitudes U_ℓ are obtained by recalling Eq.(2.46) and defining it with Eq.(2.26) as

27
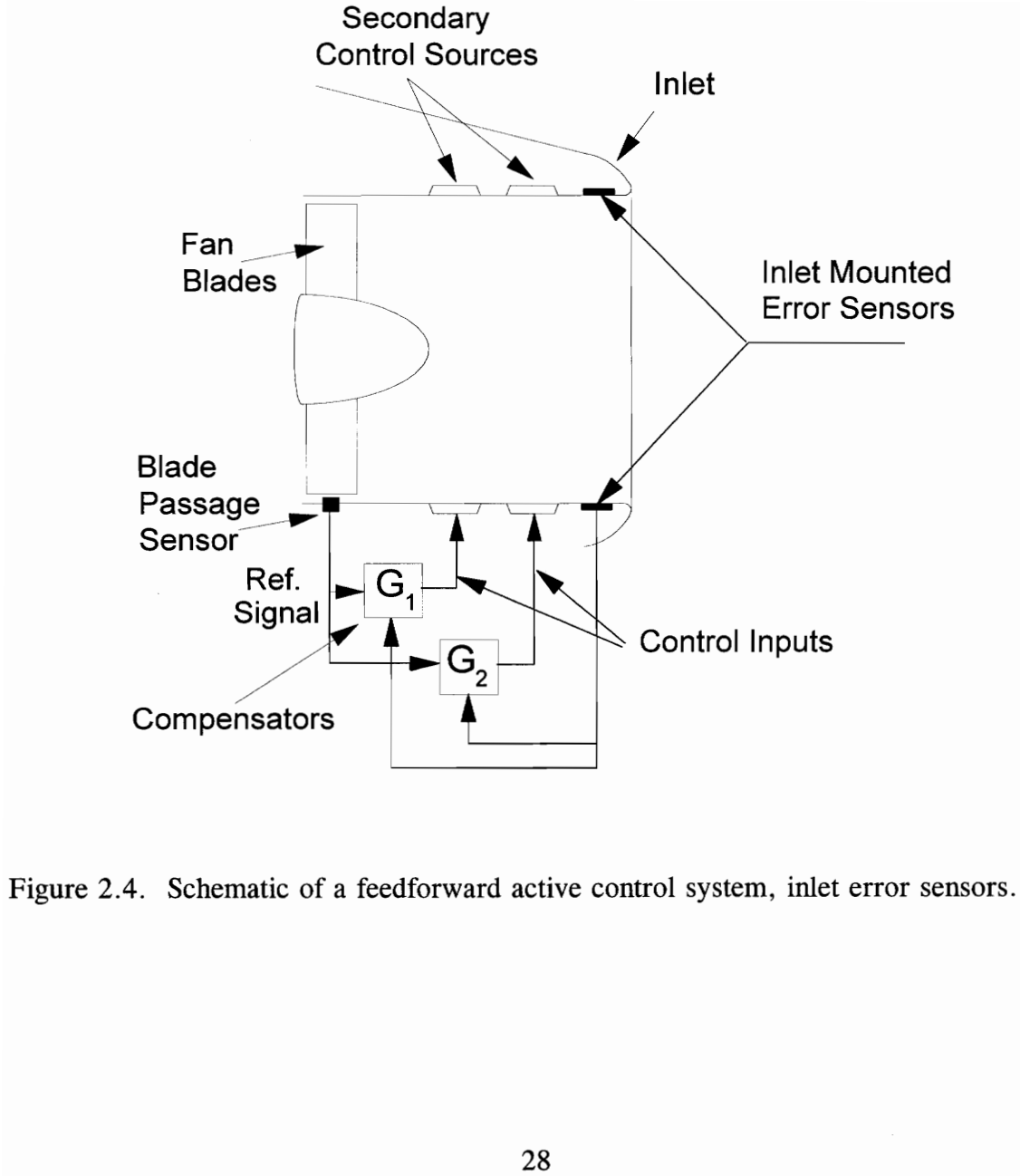
Figure 2.4. Schematic of a feedforward active control system, inlet error sensors.

$$\{U\} = -((\ [T]^T\ [T])^{-1}[T]^T\ )\ \{(P_{ff})^e_d\} \qquad (2.48)$$

The (e,ℓ) element of matrix $[T]$ is given as

$$T_{e,\ell} = \{R_e\}^T\ \{(P_{ff})^n_c\} \qquad (2.49)$$

where the components of vector $\{(P_{ff})_c^n\}$ are the far field pressure due to each point source evaluated at the error sensor location $(R_e,\ \beta_e,\ \Phi_e)$ given by Eq.(2.36). For the case of equal error sensors and control channels $(N_E = N_C)$, Eq.(2.48) reduces to

$$\{U\} = -[T]^{-1}\ \{(P_{ff})^e_d\} \qquad (2.50)$$

and all the error signals are theoretically driven to zero.

2.4.1.2   Inlet Error Sensors

The potential of using distributed transducers placed in the inlet duct as error sensors is also studied. Distributed inlet sensors have several advantages over point transducers. The ability to measure the average pressure across the face of a sensor serves to eliminate the random flow noise generated by the boundary layer typically seen in a turbofan engine. Also, the shape of the distributed error sensors could be tailored to selectively observe certain, desired modes.

An array of N_E distributed error sensors $(N_E \geq N_C)$ is assumed placed in the engine inlet duct, upstream of the array of secondary control sources, to monitor the acoustic field within the duct. In this work, the distributed error sensors are assumed to be

constructed of a piezoelectric film such as polyvinlydene fluoride (PVDF) [16,17].

Piezoelectric film consists of a polymer film which is stretched and poled through the

film thickness in an extremely high electrical field at elevated temperatures. A very thin

layer of metalization is deposited on each side of the film to provide a conductive path.

When subjected to a normal strain in any of the principle directions, an open circuit

voltage is created between the two metalized surfaces. The output from the PVDF film

is proportional to the integral of the pressure over the area of application. Different

backing configurations can be used to tailor the sensitivity of the film to the type of

measurement desired. For this study, a small piece of PVDF is assumed bonded to

acoustical foam to create an error transducer. These sensor assemblies are placed in the

engine inlet so that the PVDF film is flush with the inlet duct surface. No portion of the

sensor assembly protrudes into the flow area of the duct.

The error output generated by both the fan and the secondary control sources is

required. To determine the output from the distributed error films due to the fan noise,

Eq.(2.1) is evaluated across the surface of each film to find the average sound pressure.

Each sensor film is defined by the axial limits x_1^e and x_2^e, and circumferential limits θ_1^e

and θ_2^e, as shown in Figure 2.5. Integrating Eq.(2.1) across the surface of sensor film

e yields
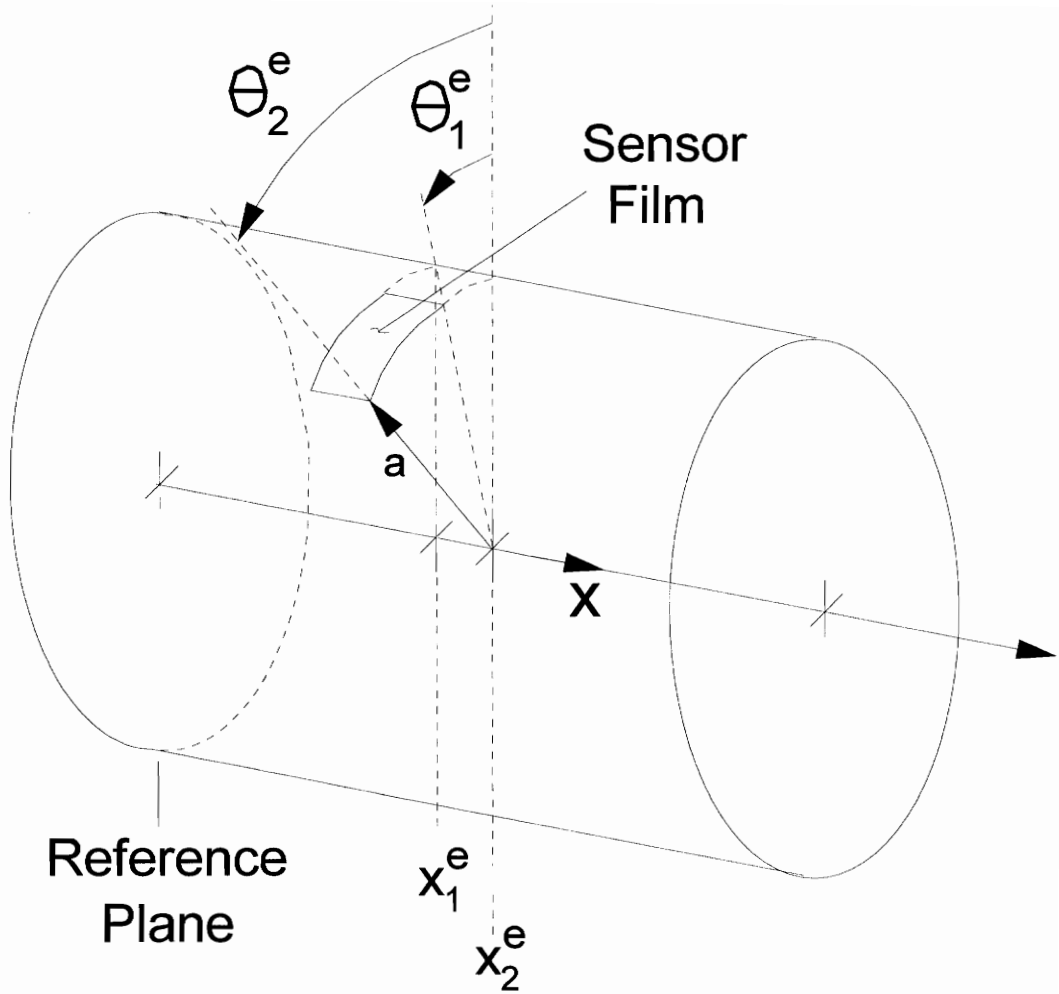
Figure 2.5. Details of inlet mounted error sensor film.

31

$$(P_i^e)_d = \alpha \sum_{m,\mu} A_{m\mu} \ J_m(k_{m\mu}a) \int_{\theta_1^e \ x_1^e}^{\theta_2^e \ x_2^e} \int e^{-im\theta} e^{-ik_x x} \ dx d\theta \qquad (2.51)$$

where α is a proportionality constant that will depend on the sensor characteristics. Separating the integrals, the integral in terms of x becomes

$$I_x = \int_{x_1^e}^{x_2^e} e^{-ik_x x} dx \qquad (2.52)$$

Completing the integration, Eq.(2.52) yields

$$I_x = \frac{i}{k_x} \{e^{-ik_x x_2^e} - e^{-ik_x x_1^e}\} \qquad (2.53)$$

Likewise from Eq.(2.51), the integral in terms of θ can be written as

$$I_\theta = \int_{\theta_1^e}^{\theta_2^e} e^{-im\theta} d\theta \qquad (2.54)$$

Completing the integration, Eq.(2.54) yields

$$I_\theta = \frac{i}{m} \{e^{-im\theta_2^e} - e^{-im\theta_1^e}\} \qquad (2.55)$$

Substituting Eqs.(2.53) and (2.55) into Eq.(2.51), the average pressure across error sensor film e due to the fan noise becomes

$$(P_i^e)_d = -\alpha \sum_{m\mu} \frac{A_{m\mu}}{k_x m} \ J_m(k_{m\mu}a) \frac{\{e^{-ik_x x_2^e} - e^{-ik_x x_1^e}\} \ \{e^{-im\theta_2^e} - e^{-im\theta_1^e}\}}{(x_2^e - x_1^e) \ (\theta_2^e - \theta_1^e) \ a} \qquad (2.56)$$

32

The error output due to a single point source can be determined by integrating Eq.(2.4) across the surface of the sensor as

$$(P_i^e)_c^n = \frac{-i\alpha}{2\pi a^2} \sum_{m,\mu} \frac{J_m(k_{m\mu}a) \, \Psi_{m\mu}(a,\theta_n)}{\Lambda_{m\mu}k_x} \int_{\theta_1^e}^{\theta_2^e} \int_{x_1^e}^{x_2^e} \cos(m(\theta - \theta_n))e^{-ik_x|x_t - x_n|} \, dxd\theta \quad (2.57)$$

Separating the integrals of Eq.(2.57), the integral in terms of x can be written as

$$I_x = \int_{x_1^e}^{x_2^e} e^{-ik_x|x - x_n|} \, dx \qquad (2.58)$$

Completing the integration, Eq.(2.58) yields

$$I_x = \frac{i}{k_x}\{e^{-ik_x|x_2^e - x_n|} - e^{-ik_x|x_1^e - x_n|}\} \qquad (2.59)$$

Likewise from Eq.(2.57), the integral in terms of θ can be written as

$$I_\theta = \int_{\theta_1^e}^{\theta_2^e} \cos(m\theta - m\theta_n)d\theta \qquad (2.60)$$

Expanding Eq.(2.60) using trigonometric identities and completing the integration yields

$$I_\theta = \frac{1}{m}\{\sin(m(\theta_2 - \theta_n)) - \sin(m(\theta_1 - \theta_n))\} \qquad (2.61)$$

Then, substituting Eqs.(2.59) and (2.61) into Eq.(2.57), the average pressure across error sensor e due to a single point source located downstream of the error sensor film can be written as

33

$$(P_i^e)_c^n = \alpha \sum_{m,\mu} \frac{J_m^2(k_{m\mu}a)}{2\pi a^2 \Lambda_{m\mu} k_x^2 m} \frac{\{e^{-ik_x(x_2^e - x_n)} - e^{-ik_x(x_1^e - x_n)}\} \{\sin(m(\theta_2^e - \theta_n)) - \sin(m(\theta_1^e - \theta_n))\}}{(x_2^e - x_1^e)(\theta_2^e - \theta_1^e)\, a} \qquad (2.62)$$

It is clear from Eqs.(2.55) and (2.62) that as the dimensions of the film are reduced, i.e. $x_2^e \to x_1^e$ and $\theta_2^e \to \theta_1^e$, the output from the distributed sensor approaches the output from a point sensor.

The optimum complex control amplitudes U_ℓ for the inlet sensing technique can then be defined as

$$\{U\} = -\left(([T]^T [T])^{-1}[T]^T\right)\{(P_i^e)_d\} \qquad (2.63)$$

Here, the (e,ℓ) element of matrix $[T]$ is given as

$$T_{e,\ell} = \{R_e\}^T \{(P_i^e)_c^n\} \qquad (2.64)$$

where the components of vector $\{(P_i^e)_c^n\}$ are the inlet pressure due to each point source evaluated at the eth error sensor film given by Eq.(2.62). For the case of equal error sensors and control channels ($N_E = N_C$), Eq.(2.63) reduces to

$$\{U\} = -[T]^{-1}\{(P_i^e)_d\} \qquad (2.65)$$

and all the error signals are theoretically driven to zero.

Chapter 3

Numerical Analysis

The purpose of the analytical model development is to uncover the mechanisms of active control as it applies to radiated fan noise. Several numerical analysis efforts are conducted in this chapter. First, the physical characteristics used throughout the numerical analysis based on previous experimental work [3-5] is presented. The acoustic disturbance created by this engine model is discussed. Predicted radiation results from the simulation of the fan noise are compared to experimentally measured pressure patterns.

The remaining sections of this chapter are dedicated to the simulation of the active noise control system. Different control source and error sensor configurations are presented and their effectiveness to attenuate the radiated fan noise is studied. System configurations with different combinations of single and multiple arrays of control sources and far field and inlet mounted error transducers are investigated. A sensitivity study is presented next. Here a formal effort is undertaken to understand the effect of parameter variations to the performance of the active noise control system. Following, the effect of mean flow present in the inlet duct on the ability to attenuate the far field noise is studied. And finally, the results of the analytical model are compared to numerical results obtained from a principle component analysis approach to the active

control of radiated fan noise [18].

To illustrate the performance of the analytical model, a turbofan engine with an inlet diameter of 0.53 meters and duct length of 1 meter is modeled. The blade passage frequency (BPF) is assumed to be 2400 Hz. The speed of sound in air, c, is 343 m/s and the density of air ρ is 1.21 kg/m^3. These parameters are based on the engine used in the experimental work of researchers at Virginia Tech [3-5]. In their work, a circumferential array of equally spaced exciter rods were placed in the inlet of a Pratt and Whitney JT15D turbofan engine upstream of the fan stage. The wake from these rods interact with the 28 fan blades to produce tones which are significantly higher in sound level than without the rod interactions. The main purpose of the rods is to excite to dominance specific acoustic modes at the blade passage frequency. The acoustic modes at the BPF excited by the interaction between the rods and the fan blades can be analytically predicted [9]. An acoustic mode, as stated in Chapter 2, is identified by the circumferential order m and radial order μ, written as (m,μ). The circumferential order, m, is determined by the interaction of B exciter rods with the 28 fan blades as

$$m = 28 - k\,B \qquad (3.1)$$

where k is an integer number. Thus, an array of 27 rods will produce the circumferential order m=1 and an array of 28 exciter rods will produce the plane wave mode m=0. In the experimental work at Virginia Tech arrays of 27 and 28 exciter rods were used to excite to dominance the first order spinning mode (m=1) and the

36

axisymmetric modes (m=0), respectively. Although the generation of both plane wave and spinning modes will be visited in an attempt to test the analytical model, only spinning acoustic modes will be assumed present in the duct for the purpose of the active control study.

The numerical investigation will include the effects of the propagating modes at the blade passage frequency from $0 \leq m \leq 5$ and $0 \leq \mu \leq 4$. The structure of the cylindrical modes for circumferential order m=0 through m=5 and radial order $\mu=0$ and $\mu=4$ are shown in Figure 3.1. A propagating mode, as described earlier, is a mode with a real axial wavenumber, k_x. Table I shows the axial wavenumbers at 2400 Hz as computed from Eq.(2.2). At a blade passage frequency of 2400 Hz, there are 17 modes above cut-on frequency as indicated in Table I that will be excited by each point source. Also from Table I it can be determined that the fan will excite to dominance the first four axisymmetric modes, m=0 and $\mu=0$, 1, 2, 3 (if 28 exciter rods are used) or the first three circumferential modes, m=1 and $\mu=0$, 1, 2 (if 27 exciter rods are used). For the purpose of this analytical study, the complex modal amplitudes of the propagating fan modes $A_{m\mu}$ are set to unity.
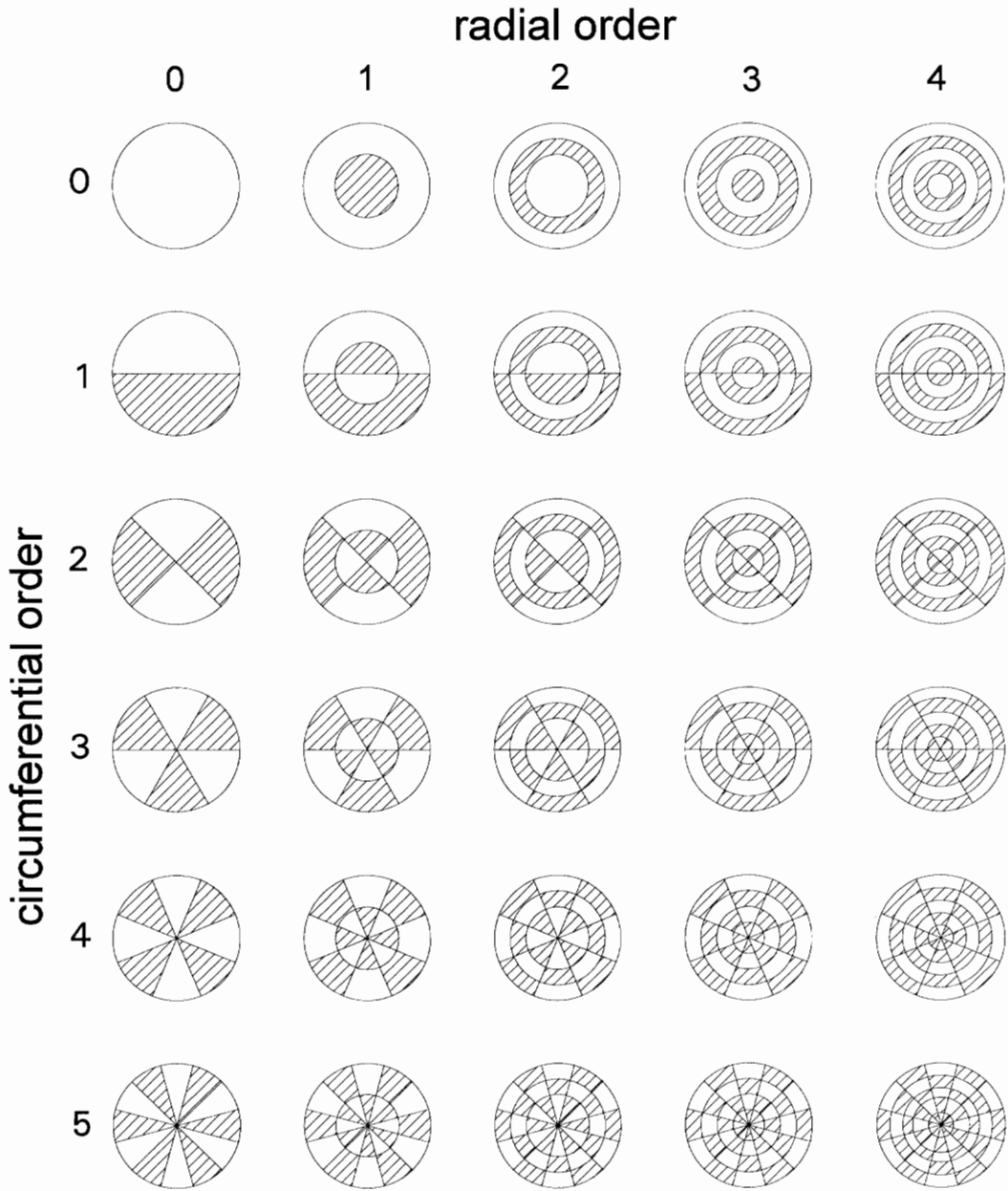
Figure 3.1. Cylindrical mode patterns for all possible modal configurations for cirumferential index m=0 through m=5 and radial index μ=0 through μ=4.

Table I: Axial wavenumber of the duct modes, k_x, at the BPF of 2400 Hz

m \ μ	0	1	2	3	4
0	43.96	41.52	35.09	21.45	i 24.37
1	43.41	39.09	29.90	i 4.45	i 34.81
2	42.43	35.94	22.75	i 23.17	i 43.29
3	41.01	31.89	9.92	i 33.14	i 50.73
4	39.11	26.58	i 18.89	i 41.16	i 57.59
5	36.71	18.89	i 29.23	i 48.31	i 64.02

3.1 Model Validation

The analytical model is tested for correct operation. This effort in model verification involves simulating the fan disturbance alone. The modes generated by the fan are restricted to the plane wave ($A_{00}=A_{01}=A_{02}=A_{03}=1.0$) and first order spinning modes ($A_{10}=A_{11}=A_{12}=1.0$) which propagate at the fan blade passage frequency, as described earlier.

With the axisymmetric modes present in the duct, the far field radiation should be fairly uniform in shape, with no nodal lines of zero pressure existing. On the other hand, with the first order spinning modes excited to dominance in the duct, the far field radiation pattern should exhibit a notch in the center corresponding to the nodal line of the cylindrical mode pattern. Figure 3.2 contains the horizontal cross-section of the
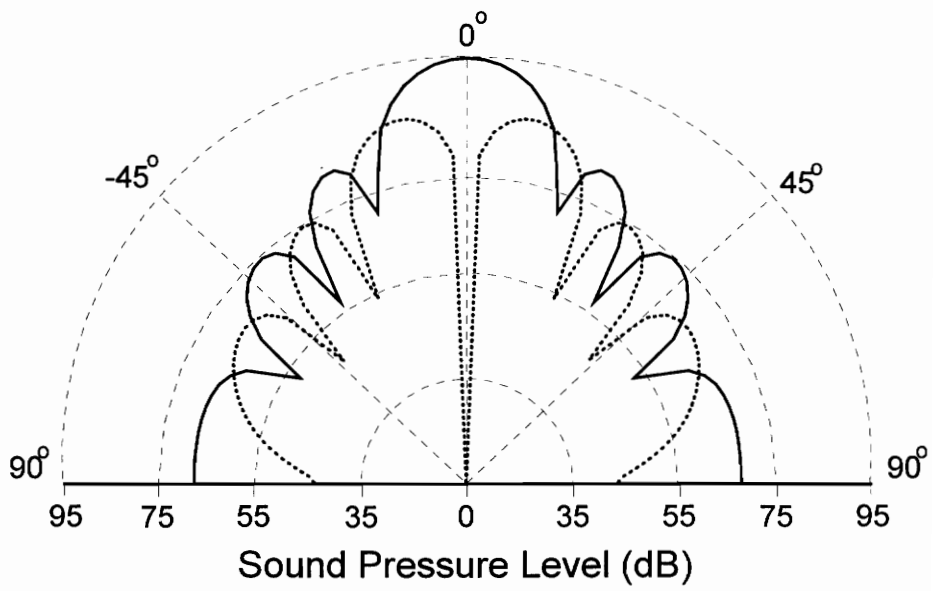
Figure 3.2. Vertical cross-section of radiation directivity of fan noise for axisymmetric modes (solid-line) and first order spinning modes (dotted-line).

40

radiation directivity for the axisymmetric modes (solid-line) and the first order spinning modes (dotted-line).

The performance of the analytical model is now compared to the results obtained experimentally by Thomas et. al. [3-5]. This experimental work was conducted on a Pratt and Whitney JT15D turbofan engine located in the Turbomachinery Laboratory of the Virginia Tech Airport. The experimental results examined here involve the comparison of the far field radiation noise levels due to the fan disturbance. The investigators measured the radiated far field sound pressure at 10° intervals about the horizonal plane in front of the engine inlet. The sound pressure measurements were taken at a radial distance of 1.5 m from the open section of the engine.spinning modes. The fan blade passage frequency was measured as 2375 Hz.

The analytical model was simulated to match the experimental parameters. The results of the comparison for both the axisymmetric modes and the spinning modes are presented in Figure 3.3. The hatched bars represent the experimental results and the solid bars represent the analytical results. It should be noted that the amplitude of the analytical results were normalized with the experimental data to more closely match the magnitude of the actual far field sound pressure levels in the centerline regions of the engine. The results presented in Figure 3.3 can be inspected for similarities in overall sound pressure patterns and trends. The radiation directivities of Figure 3.3(a) match closely across the traverse angle. Similar reduction trends in sound pressure level are seen at ±50° and nearly identical pressure results are seen at the sidelines. The sound
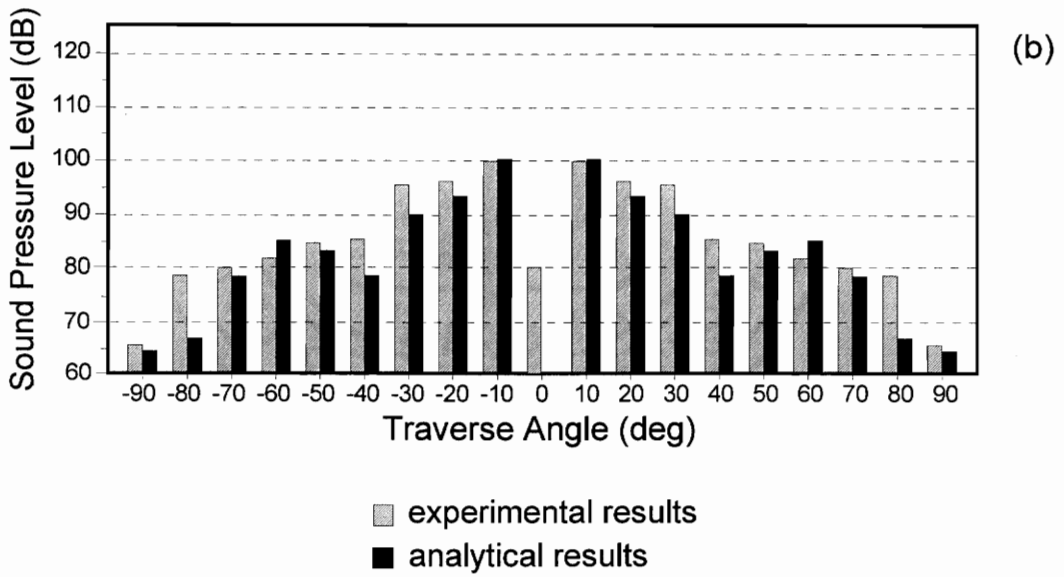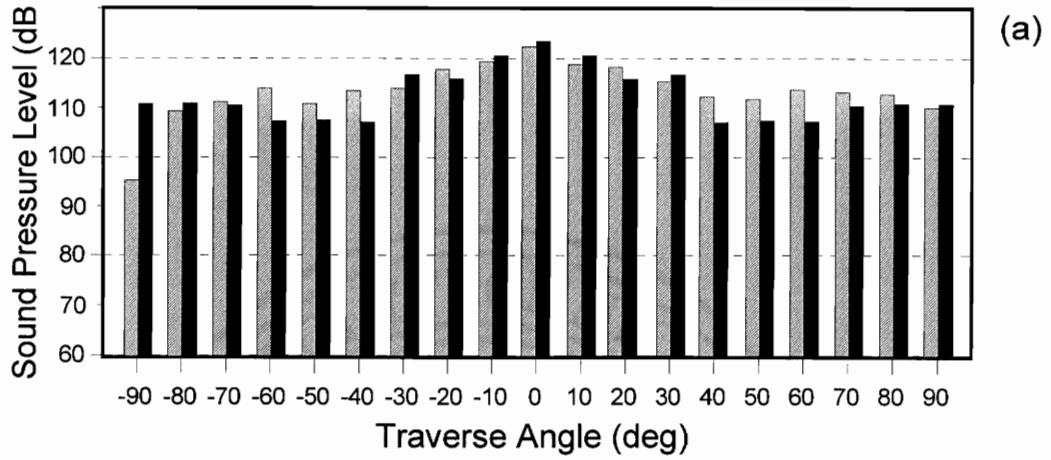
Figure 3.3. Comparison of experimental and analytical results; (a) 28 exciter rods, (b) 27 exciter rods.

42

pressure at the extreme sidelines also agree for the case of 27 exciter rods. In Figure 3.3(b), the sound pressure trends across the traverse angle are also similar, with notches in the radiated sound pressure appearing at $\pm 40°$ for both the experimental and analytical data. It should be noted that the lack of analytical data at a traverse angle of $0°$ for the spinning mode comparison is contributed to the fact that the analytical model introduced only purely first order spinning modes generated by the fan.

An important conclusion can be made from the comparison of experimental and analytical fan radiation data. The analytical model was simulated with modal amplitudes of unity. The value of $A_{m\mu}$ could be different, both in magnitude and phase content, for each mode excited by the fan. For instance, if it was determined that an engine design would excite the mode (1,0) to a greater magnitude than the other propagating modes, the modal amplitudes of the analytical model could be varied accordingly. The results presented in Figure 3.3(a,b) suggest , however, that the modal amplitudes of the engine match those selected for the analytical model. Thus, the modal amplitudes of unity for this study are justified.

3.2   Single Axial Array Control Configuration - Far Field Error Sensors

The control source configuration chosen for the numerical analysis is a six channel ($N_C = 6$) system comprised of twelve evenly distributed point sources ($N_S = 12$)

located within the periphery of the inlet duct, with the first point source placed at $\theta = 0°$.

The single axial plane of control sources is placed upstream of the fan. The first row of the control configuration matrix [R] is $\{R_1\} = \{1,0,0,0,0,0,-1,0,0,0,0,0\}$, indicating that control channel one, U_1, drives control sources 1 and 7 with a 180° phase difference. Control channel two is described by $\{R_2\} = \{0,1,0,0,0,0,0,-1,0,0,0,0\}$ indicating that control sources 2 and 8 are out-of-phase and driven by the second control signal U_2. The remainder of [R] follows the set pattern. This configuration is selected for best coupling with the $m = 1$ duct modes produced by the fan.

To quantify the performance of a chosen control system, the resulting controlled far field sound pressure is computed over a hemisphere of radius 1.5 m placed in front of the open section of the inlet duct. The overall sound power level is then obtained by integrating the intensity over this hemisphere. This sound power level is compared to the uncontrolled fan noise sound power level to determine the performance of the controlled system.

The resulting far field radiation from the simulation of the fan disturbance alone, measured at a distance of 1.5 m from the duct opening, is shown in Figure 3.4. This plot represents the three-dimensional radiation directivity due to the fan in an uncontrolled state. Evidence of a spinning mode is presented by the existence of a notch at the center of the directivity pattern. A pressure decrease at approximately 45° off the engine axis between two major lobe patterns, as well as a lower pressure distribution of the fan noise at the extreme sidelines are clearly seen. The total radiated uncontrolled
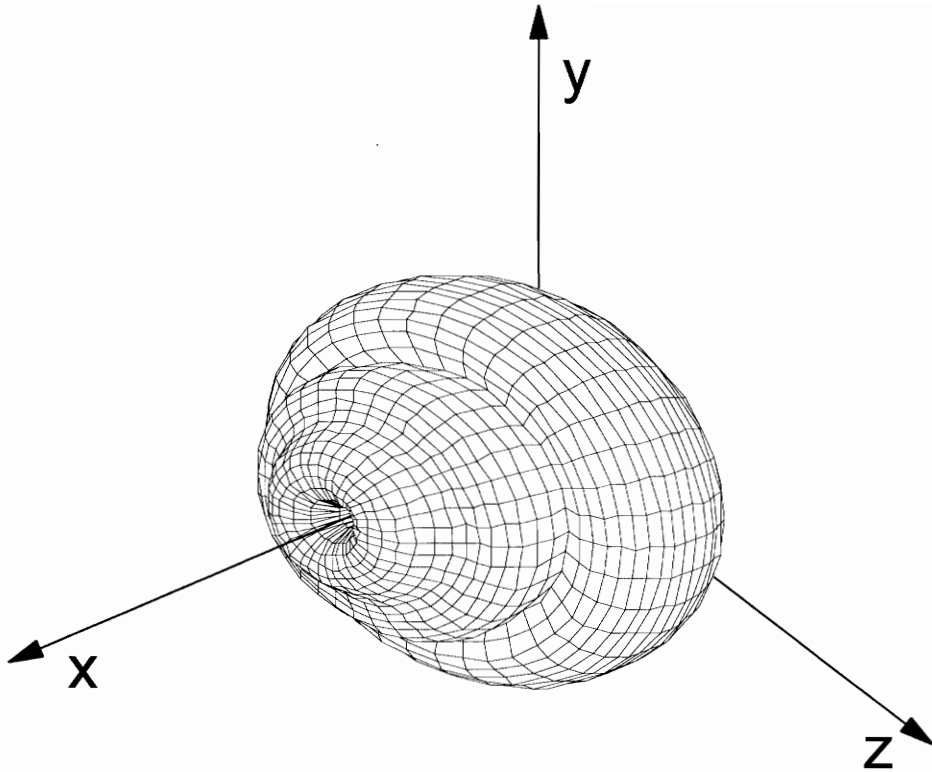
Figure 3.4. Radiation directivity of uncontrolled fan noise for an engine modeled with an inlet diameter of 0.53 meters, duct length of 1 meter and blade passage frequency of 2400 Hz.

sound power level is 87.56 dB.

A parametric investigation of the analytical model was conducted to study the performance of different control system configurations. A schematic of the parametric study configuration is shown in Figure 3.5. The axial position of the control source array described earlier is stepped along the duct length from 0.05 m to 0.95 m upstream of the fan in 0.05 m increments. Six error sensors (N_E=6) are used to measure the far field radiation. The six point error sensors are distributed around the engine centerline axis, with the first sensor at β=0° and each of the remaining sensors placed at 30° intervals. The error sensors are stepped through varying angular positions Φ as measured from the engine centerline axis. All of the six error sensors are moved such that each sensor maintains an equal angular distance Φ from the engine axis. The six error sensors are placed at a radial distance of R=1.5 meters from the open section of the inlet duct. The radial distance, as well as the control configuration matrix [R] and BPF are not varied. It is important to remark that for this case of equal number of control inputs and error outputs, the error signals will be driven to zero.

The results of the parametric study for a single axial array of control sources and far field error sensors are plotted in Figure 3.6. This figure presents the overall global attenuation achieved by a specified control configuration, with positive values along the z-axis representing a decrease in overall radiated sound power from the original uncontrolled fan noise due to the destructive interference of the secondary control sources. A negative value along the z-axis implies that an increase in radiated sound
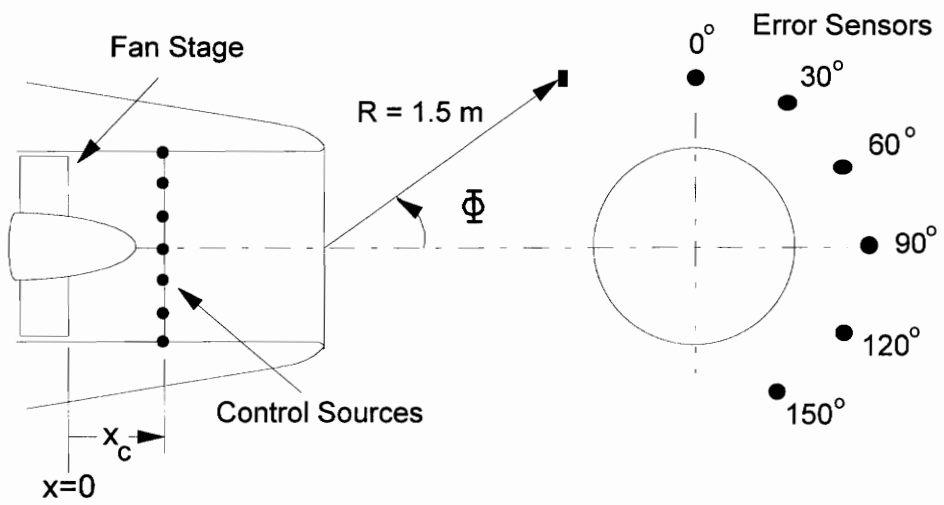
46

Figure 3.5. Schematic for parametric investigation, single axial array of control sources, far field error sensors.
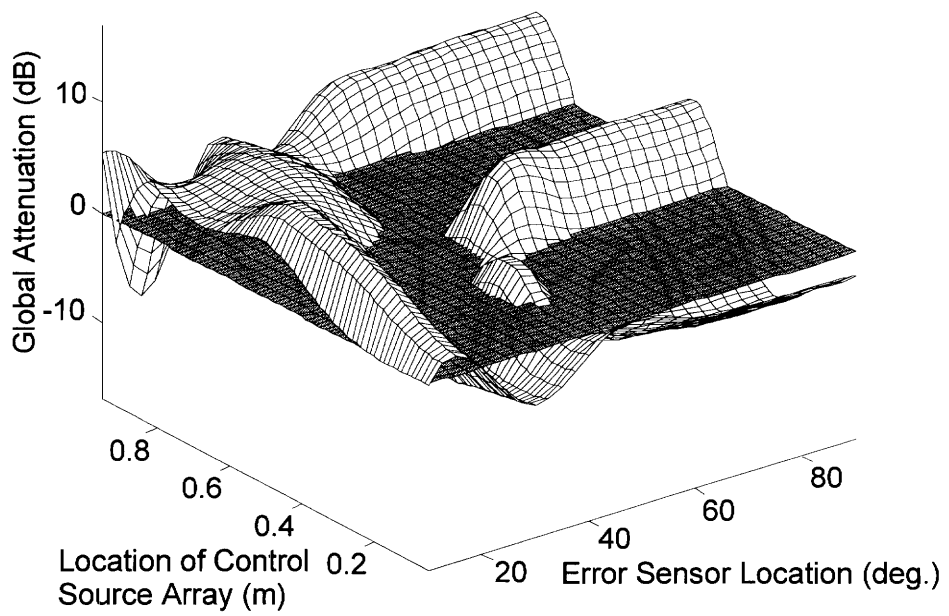
Figure 3.6. Global attenuation results for single axial control source configuration and far field error sensors.

power has resulted with the addition of the secondary control source contribution even though the error signals are driven to zero, i.e. spillover effects. The darkened plane, or reference plane, appearing in the figure represents the original sound power of the uncontrolled fan noise. The y-axis represents the axial position of the secondary control source array with respect to the fan station. The x-axis represents the angular position of the far field error sensors relative to the engine centerline axis. The best performance, or greatest radiated power attenuation, is achieved with the secondary control source array placed 0.5 m upstream of the fan and the error sensors placed 20° off the engine axis. This configuration offers a reduction in overall sound power of 6.38 dB, or a total radiated sound power level of 81.18 dB. It can be noted that in Figure 3.6 there are large areas appearing below the reference plane, representing configurations in which the overall sound power has increased with the use of the active control system. It can be concluded that the location of the control sources and error sensors is very important and sensitive to changes. This is in spite of the use of error sensors that directly measure far field pressure.

For the "best-case" single axial array control source configuration and error sensor locations described above, the complex control inputs U are calculated. These control inputs are plotted in the complex plane shown in Figure 3.7. The control inputs display equal magnitude and an equal phase angle between consecutive inputs corresponding to the angular separation of the control channels. It is shown in Appendix A that this control system structure generates only first order circumferential spinning

49
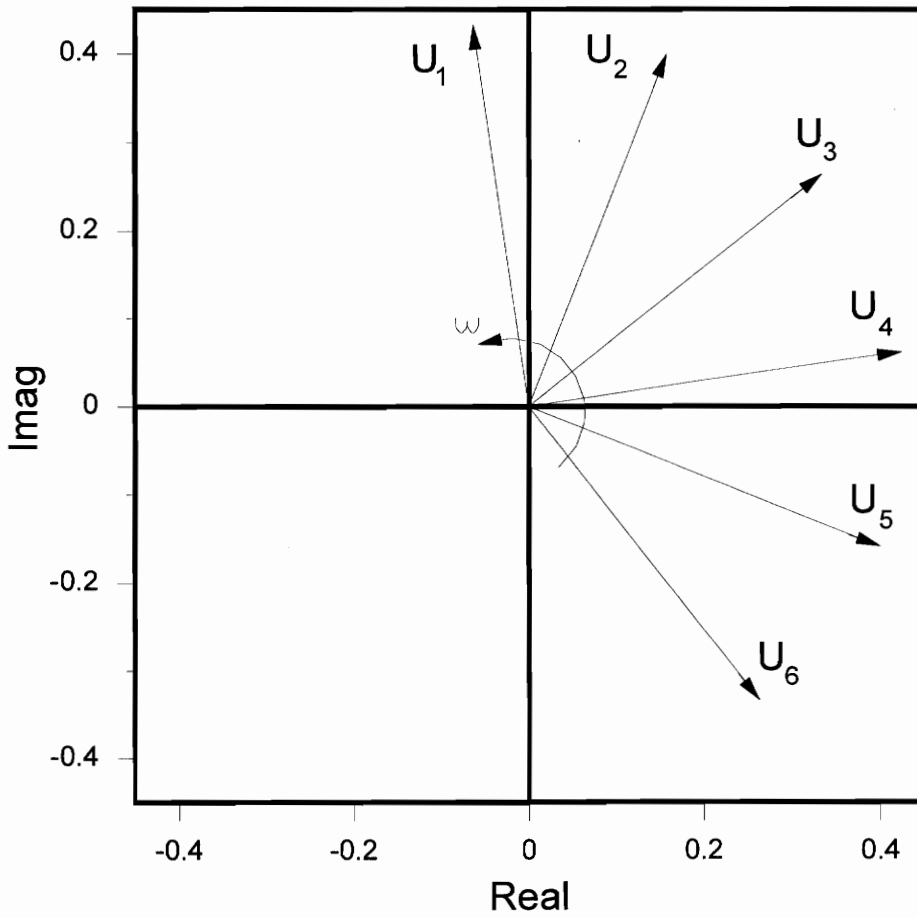
Figure 3.7. Complex control inputs for single axial control source array and far field error sensors.

mode patterns, turning at frequency ω. To understand how the complex control inputs couple into each of the three propagating fan modes the control inputs were broken down into their modal components. This was accomplished by running the analytical model for each fan mode separately. Figure 3.8 presents the modal breakdown of the complex control input U_1. It can be implied from Figure 3.8 that the complex control inputs couple strongly into the (1,0) mode as seen by the vector $U_1(1,0)$. The control inputs couple less strongly into the (1,1) and (1,2) modes suggesting that these modes may be more difficult to attenuate with the chosen arrangement of control sources.

The resulting radiation directivity for the controlled system is shown in figure 3.9. The symmetrical notch in the pressure pattern at 20° off the engine axis is created by the controller driving the error sensor signals to zero. This three-dimensional view of the controlled engine noise reveals that the axisymetric pattern of the acoustic field has been preserved using the selected error sensor configuration. A vertical cross-section taken from the radiation directivity plot is shown in Figure 3.10. The solid line of this two-dimensional radiation plot represents the uncontrolled fan noise while the dashed-line represents the controlled field. In Figure 3.10, it can more clearly be seen that by placing the error sensors at 20° off the engine axis the pressure in this region is reduced to zero. It is also evident that nearly global control of the fan noise is achieved.

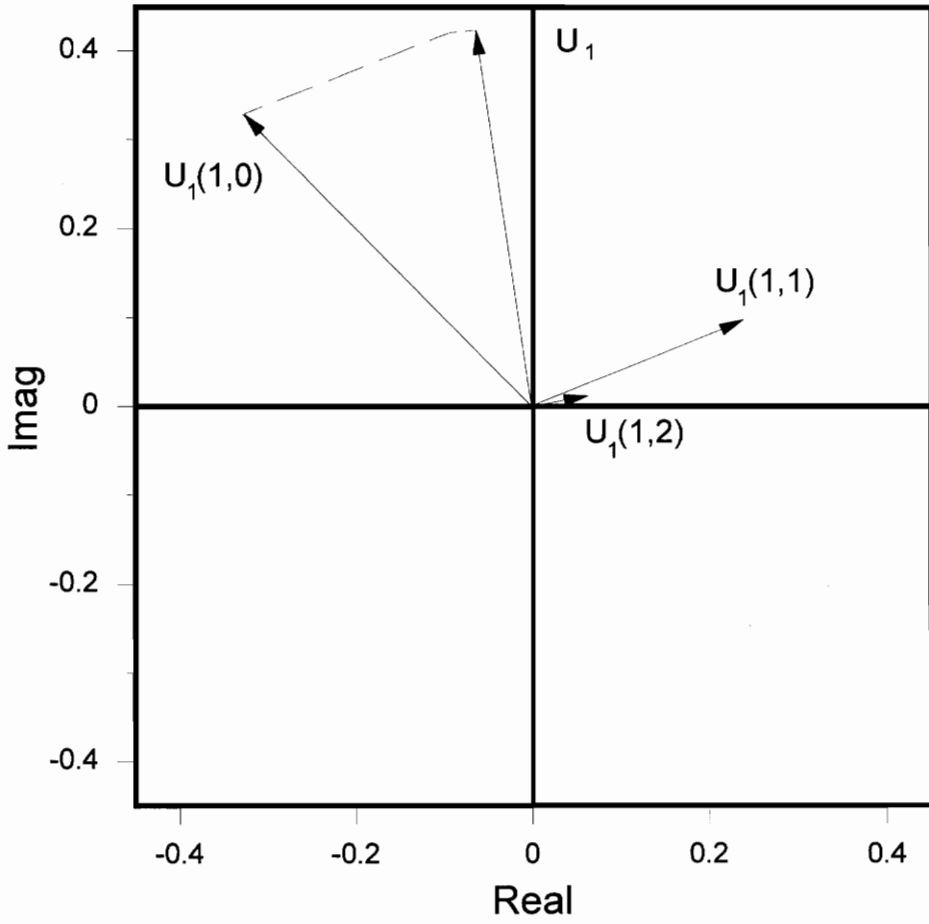Figure 3.8. Modal breakdown of complex control inputs, single axial control source array and far field error sensors.
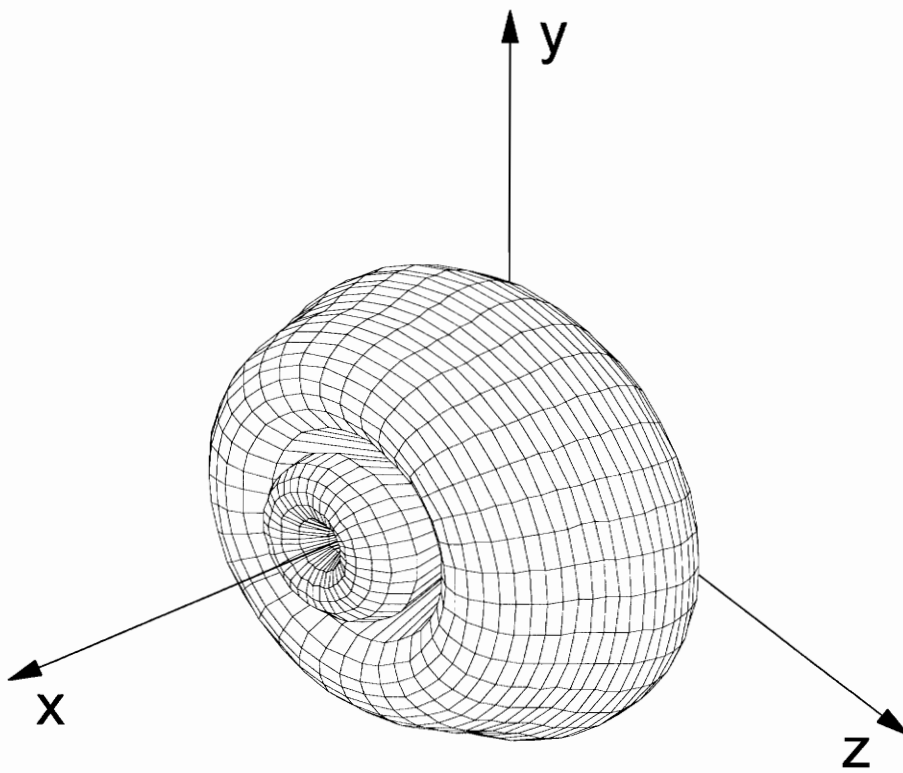
Figure 3.9. Radiation directivity of controlled fan noise using best-case single axial control source array and far field error sensor configuration.
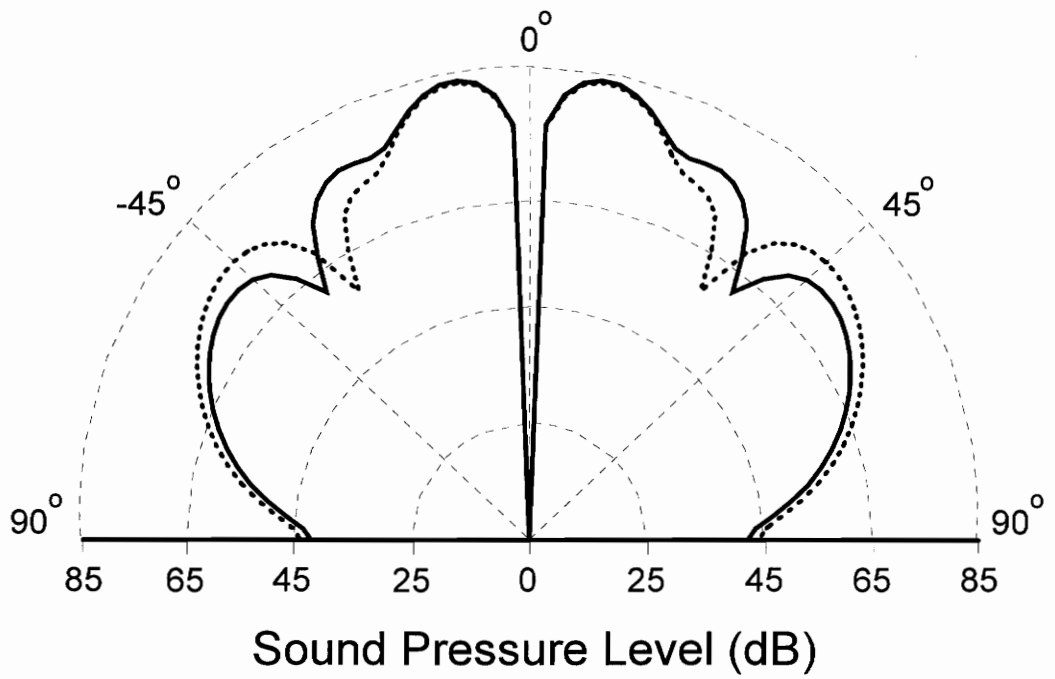
Figure 3.10. Vertical cross-section of radiation directivity of controlled fan noise for single axial control source, far field error sensors.

3.3 Multiple Axial Array Control Configuration - Far Field Error Sensors

The potential to control the fan noise using a multiple axial control source array configuration is now investigated. The arrangement of control sources within a single array, i.e. number of evenly spaced point sources, dictate the ability to couple with the circumferential modes. In fact, it has been shown that 2m is the minimum number of point sources needed to couple with the mth order spinning mode [6]. Conversely, in order to couple with the radial modes, multiple arrays of control sources must be used and placed at different axial locations within the duct.

The control system for this effort is shown in Figure 3.11. To the original control source band used in the single array study, comprised of channels 1 through 6, a second control source band, comprised of channels 7 through 12 is added. This second control source array is a mirror image of the original array and is driven through a similar configuration matrix. Six additional error sensors are also required. These point sensors are placed in the same pattern around the circumference of the engine as the original six. The second set of error sensors is placed at larger angular positions off the engine centerline axis than the original set.

The parametric investigation for this multiple axial array configuration is considerably more involved. There now exists four variables to modify in the parametric investigation. The variables are the axial location of the two control source arrays placed

Figure 3.11. Schematic for parametric investigation, multiple axial arrays of control sources, far field error sensors.

56

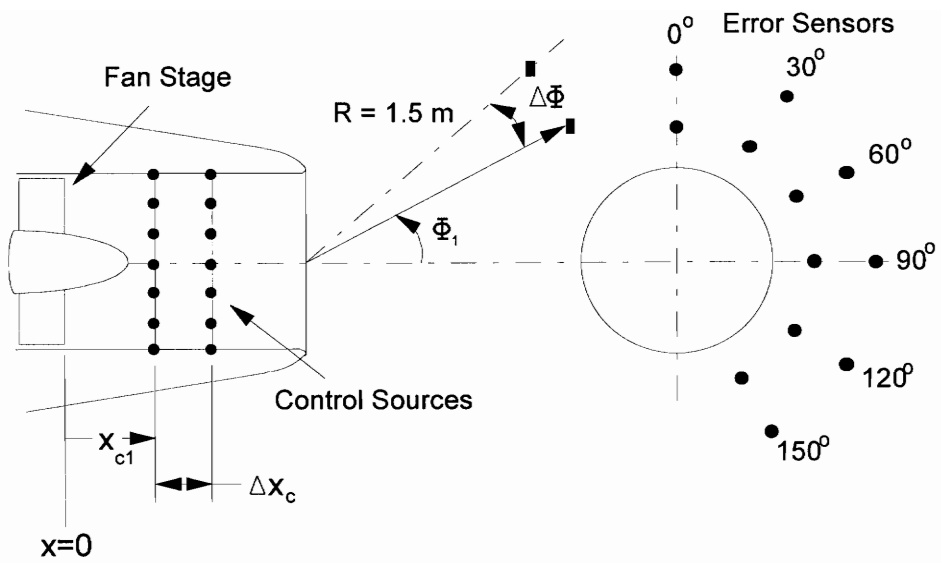upstream of the fan stage and the angular locations of the two sets of error sensors. For this study, the axial location of one control source station is set (the array closest to the fan) and the axial distance between the first station and the second array is varied. Likewise, the location of one group of error sensors is set (closest to the centerline axis) and the angular distance between the first and second groups of error sensors is varied. A single three-dimensional plot cannot display the results of four changing variables. However, sound power level reduction plots can be obtained as a function of the position of the first control array x_{c1} and angular position of the first error sensor group Φ_1 for given values of Δx_c (relative axial position of second control array) and $\Delta\Phi$ (relative angular positions of second error sensor group). Figures 3.12 through 3.14 display sample parametric study results. These plots again indicate the importance of the proper configuration of the active control system. The "best-case" multiple axial array configuration using far field error sensors can be determined from Figure 3.12. Figure 3.12 presents the global attenuation for all possible control configurations with an axial distance between control source stations of 0.25 m and an angular difference between error sensor sets of 30°. The best performance occurs with the first and second control source arrays placed at 0.60 m and 0.85 m, respectively. The corresponding error sensor locations has the first and second sets of error sensors at 10° and 40°, respectively. The global attenuation for this "best-case" scenario is 27.99 dB, resulting in an overall sound power level of 59.57 dB.

The complex control inputs of the multiple array, twelve channel system are

57

Figure 3.12. Global attenuation results for multiple control source arrays and far field error sensors; $\Delta x_c = 0.25$ m, $\Delta\Phi = 30°$.
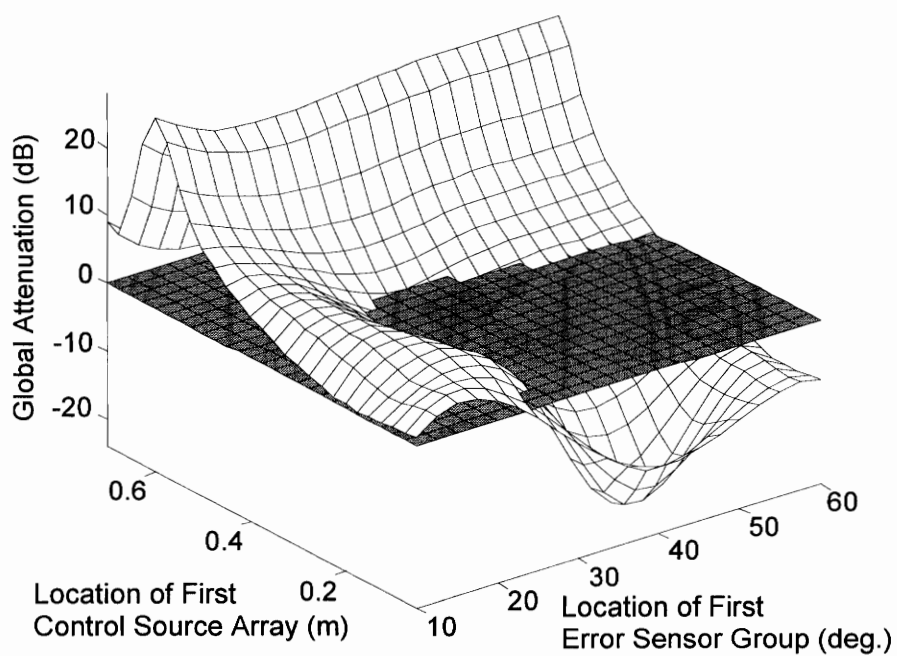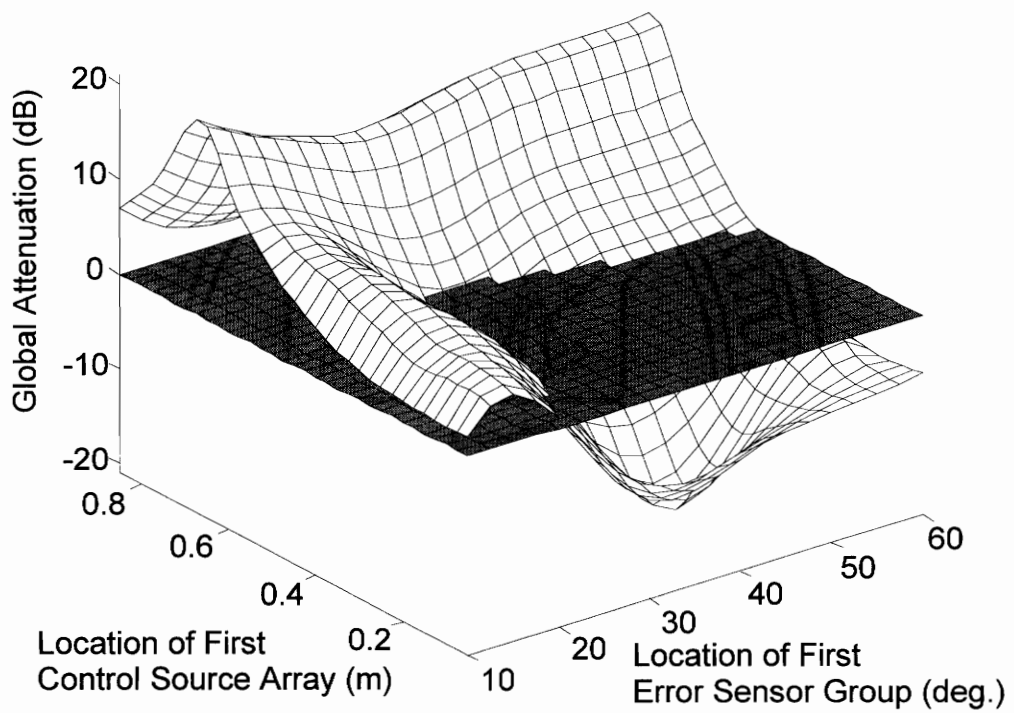
Figure 3.13. Global attenuation results for multiple control source arrays and far field error sensors; $\Delta x_c = 0.10$ m, $\Delta\Phi = 30°$.
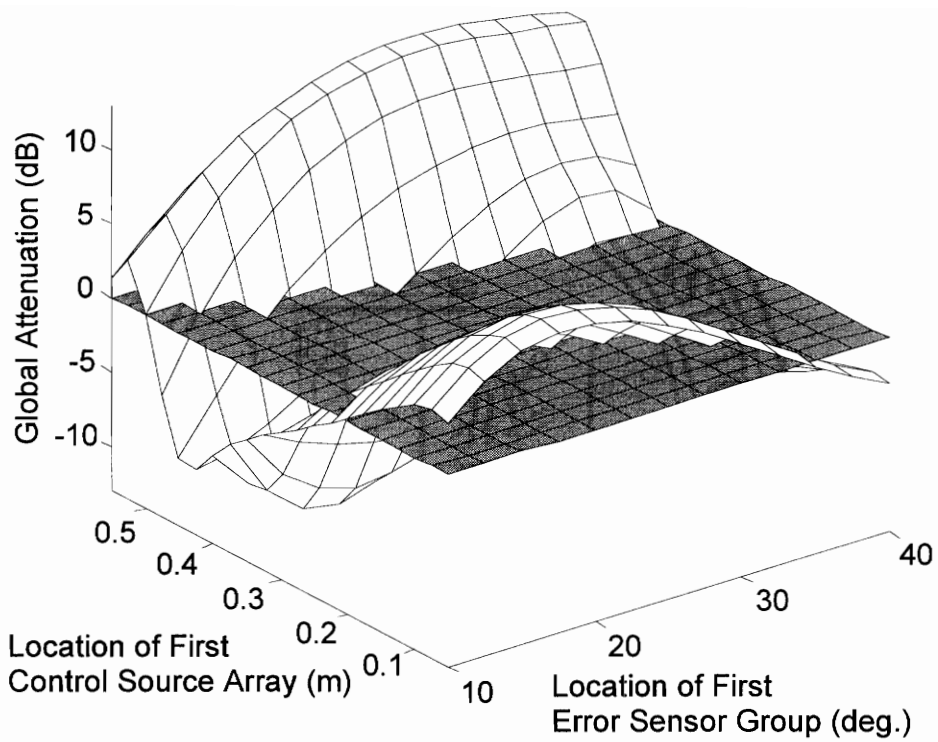
Figure 3.14. Global attenuation results for multiple control source arrays and far field error sensors; $\Delta x_c = 0.40$ m, $\Delta\Phi = 50°$.

presented in Figure 3.15. The control inputs reveal that a spinning mode pattern has been achieved by each axial station of control sources, with the magnitude and phase of each set differing due to the location of each band within the duct. Figure 3.16 presents the modal breakdown of the complex control inputs for each control source array, represented by U_1 and U_7. It is evident from Figure 3.16 that the two axial arrays of control sources couple into the propagating fan modes with different magnitudes and phase. A vertical cross-section taken of the radiation directivity, seen in Figure 3.17, reveals that global control was achieved. The solid- and dotted-lines of Figure 3.17 represent the uncontrolled fan noise and controlled field, respectively. Notches at the error sensor locations are clearly seen. The reduction in sound pressure level in the center regions of the far field is much greater when compared to the results of the single array in Figure 3.10. This is due to the larger coverage of the far field by the error sensors. It can be concluded from this result that a control scheme consisting of error sensors covering most or all of the area in front of the engine would be equivalent to minimizing the total radiated acoustic power.
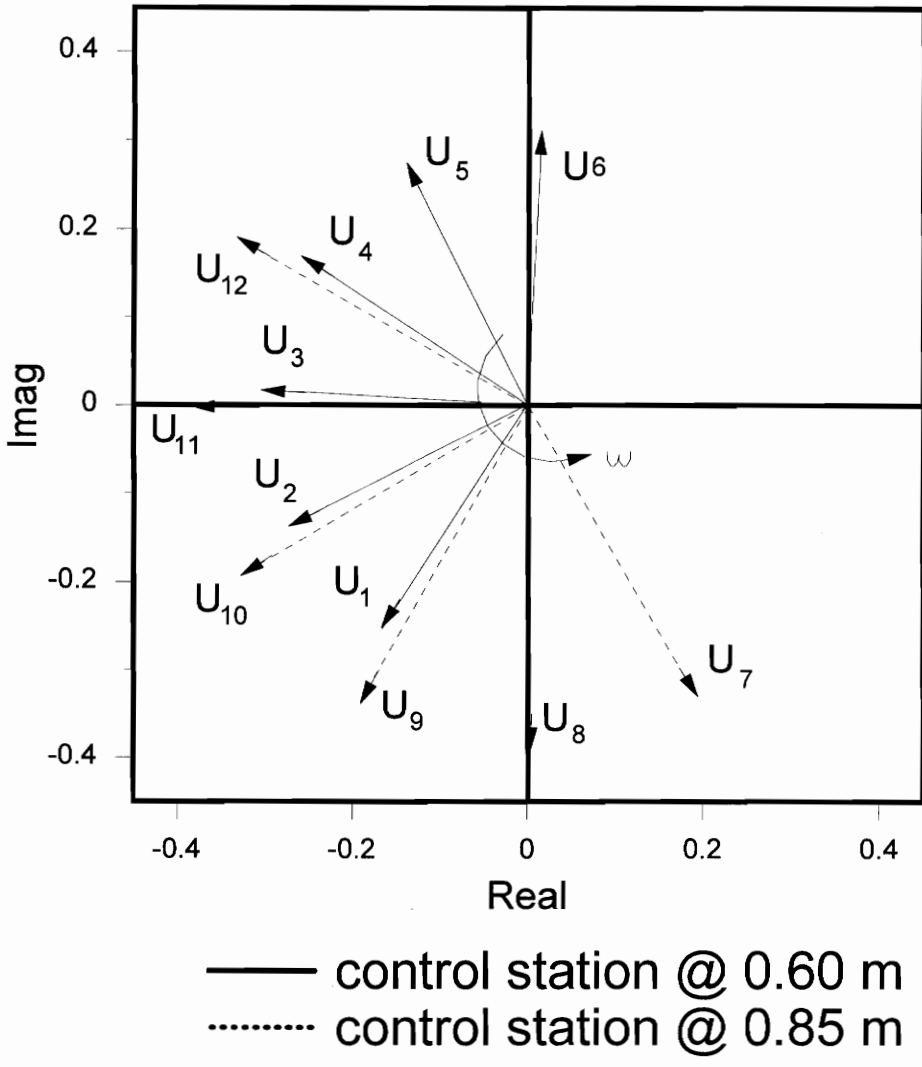
Figure 3.15. Complex control inputs for best-case multiple axial control source arrays using far field error sensors.
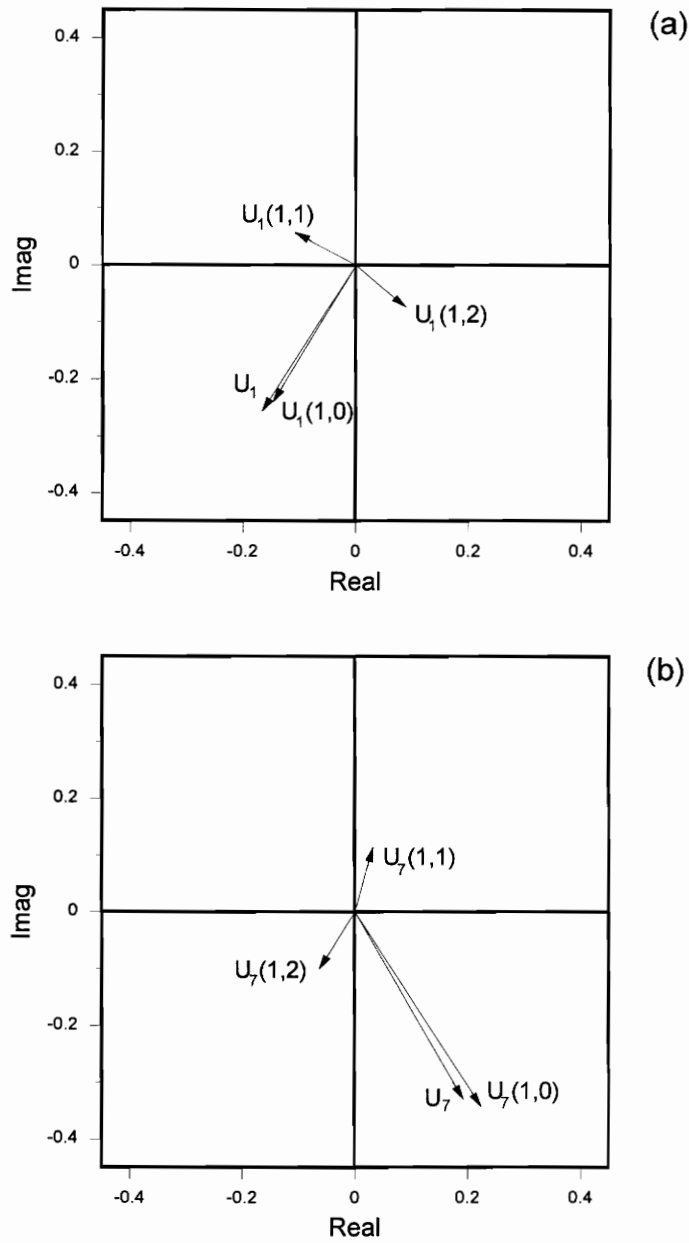
Figure 3.16. Modal breakdown of complex control inputs for multiple control source array configuration; (a) control source array at $x_{c1} = 0.60$ m and (b) control source array at $x_{c2} = 0.85$ m.

63
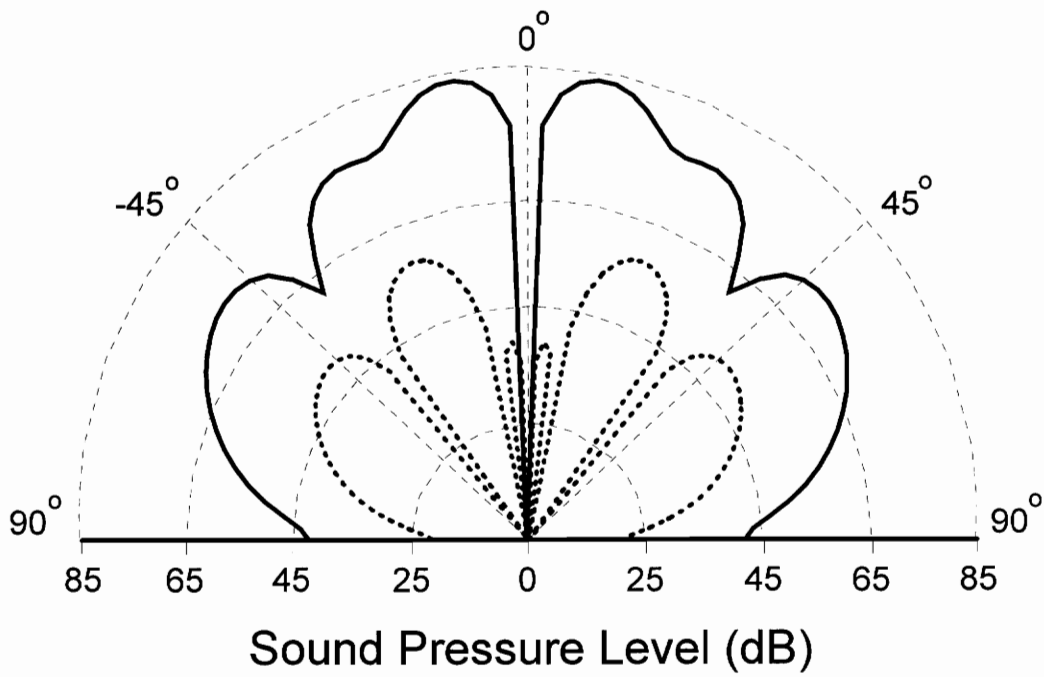
Figure 3.17. Vertical cross-section of radiation directivity of controlled fan noise using multiple control source arrays and far field error sensors.

3.4 Single Axial Array Control Configuration - Inlet Error Sensors

The next section of work investigates the potential of active control of inlet radiated tonal noise using distributed error transducers placed in the engine inlet as opposed to the point sensors placed in the far field. The basic control source configuration is similar to that used in the far field investigation and for the same reason, consisting of twelve evenly distributed point sources ($N_S = 12$) located within the periphery of the inlet duct, with the first point source placed at $\beta = 0°$. The single axial plane of control sources is placed upstream of the fan. The first row of the control configuration matrix [R] is $\{R_1\} = \{1,0,0,0,0,0,-1,0,0,0,0,0\}$, indicating that channel one drives control sources 1 and 7 with a 180° phase difference. Channel two is described by $\{R_2\} = \{0,1,0,0,0,0,0,-1,0,0,0,0\}$ with the remainder of [R] following the set pattern. Each point source is again assumed to excite all modes which propagate at the fan blade passage frequency.

Six error sensor films ($N_E = 6$) are used to measure the acoustic field within the inlet duct. The six distributed error sensors are placed on the periphery of the inlet duct upstream of the array of secondary control sources ($x_{e1} > x_{c1}$). Each sensor film is 0.05 m wide, with the first film covering the area from $\theta = 0°$ to $\theta = 30°$, the second film from $\theta = 30°$ to $\theta = 60°$ and the remaining four sensors following the set pattern. A schematic of the inlet sensor study is presented in Figure 3.18. This configuration of
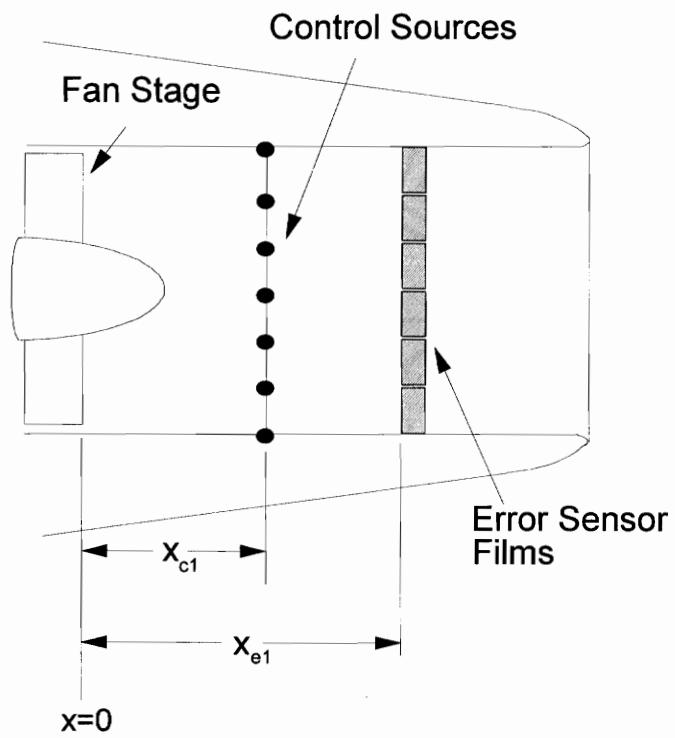
Figure 3.18. Schematic for parametric investigation, single axial array of control sources, inlet mounted distributed error sensors.

error sensors is based on experimental work currently being conducted at Virginia Tech.

A parametric investigation for the single axial array configuration is conducted to determine the optimum system configuration. The variables of the study are the axial location of the secondary control source array and the axial position of the distributed error sensor array. The position of the error sensor array is always maintained upstream of the control sources. For the purpose of the parametric study, the overall sound power of the resulting radiated sound field is determined for all possible combinations of control source array and error sensor array locations. The attenuation results of the single axial array parametric investigation using inlet mounted distributed error sensors are presented in Figure 3.19. As before, a positive value along the z-axis of Figure 3.19 represents a global attenuation of the radiated fan noise, where as a negative value along the z-axis represents an increase or spillover of acoustic energy. The y-axis represents the axial location of the control source array and the x-axis represents the location of the error sensor array, both measured relative to the fan stage. The closest the control source array is allowed to get to the fan stage is 0.05 m. The leading edge of the error sensor array is only allowed to get as close as 0.1 m from the fan stage, corresponding to a minimum axial distance between the control sources and error sensor films of 0.05 m minimum. Inspection of Figure 3.19 reveals that placement of the control source and error sensor arrays relative to the fan stage is not as critical as the relative distance between each array. The pattern in Figure 3.19 suggests that good attenuation is observed if the distance between control source and error sensor arrays is kept at

67
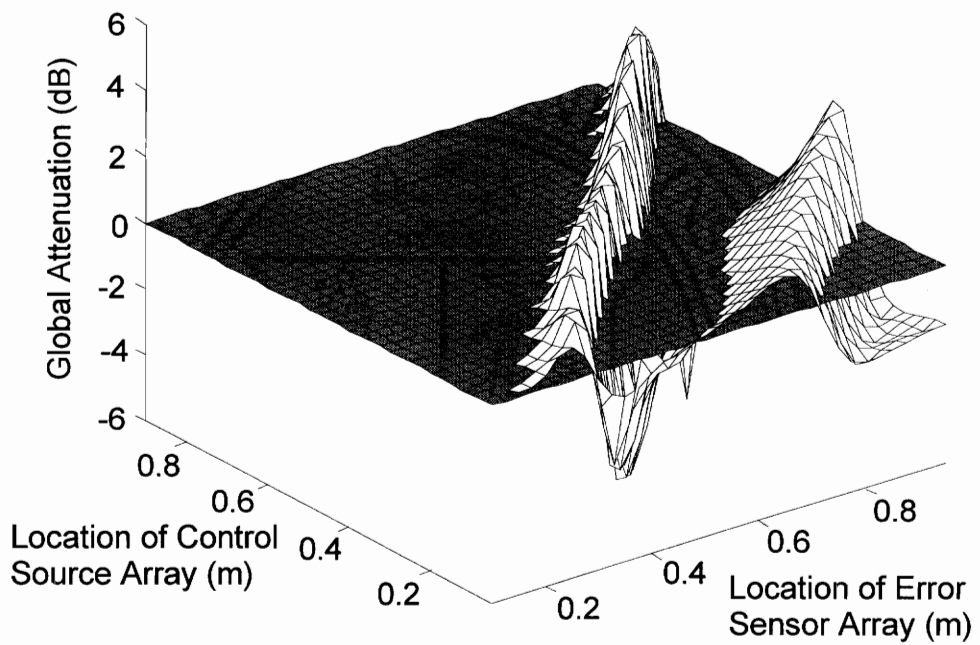
Figure 3.19. Global attenuation results for single axial control source array and inlet error sensor configuration.

68

approximately 0.1 or 0.7 m.

The best performance with a single array of control sources and inlet error sensors is achieved with the control source array placed 0.60 m upstream of the fan and the leading edge of the error sensor array placed 0.80 m upstream of the fan. The total radiated sound power level with active control is 83.38 dB, resulting in an attenuation of 4.18 dB. This attenuation can be compared to the 6.38 dB achieved with the single axial array/far field error sensor study of section 3.2.

Using the control source configuration and error sensor film locations described above, the complex control inputs are calculated. These control inputs are plotted in the complex plane shown in Figure 3.20. The control inputs display equal magnitude and an equal phase angle between consecutive inputs corresponding to the angular separation of the control channels. Again, it is easy to show that this control system structure generates only first order circumferential spinning mode patterns, turning at frequency ω (App. A). It has also been shown earlier that this type of structure preserves the axisymetric pattern of the acoustic field. Figure 3.21 presents the modal breakdown of the complex control input U_1. Again it can be seen that the control inputs couple into each fan mode with different magnitudes and phase.

A vertical cross-section taken from the radiation directivity plot is shown in Figure 3.22. The solid line of this two-dimensional radiation plot represents the uncontrolled fan noise while the dashed-line represents the controlled field. It is evident that global control of the fan noise is not achieved.

69

Figure 3.20. Complex control inputs for best-case single axial array configuration using inlet mounted error sensors.
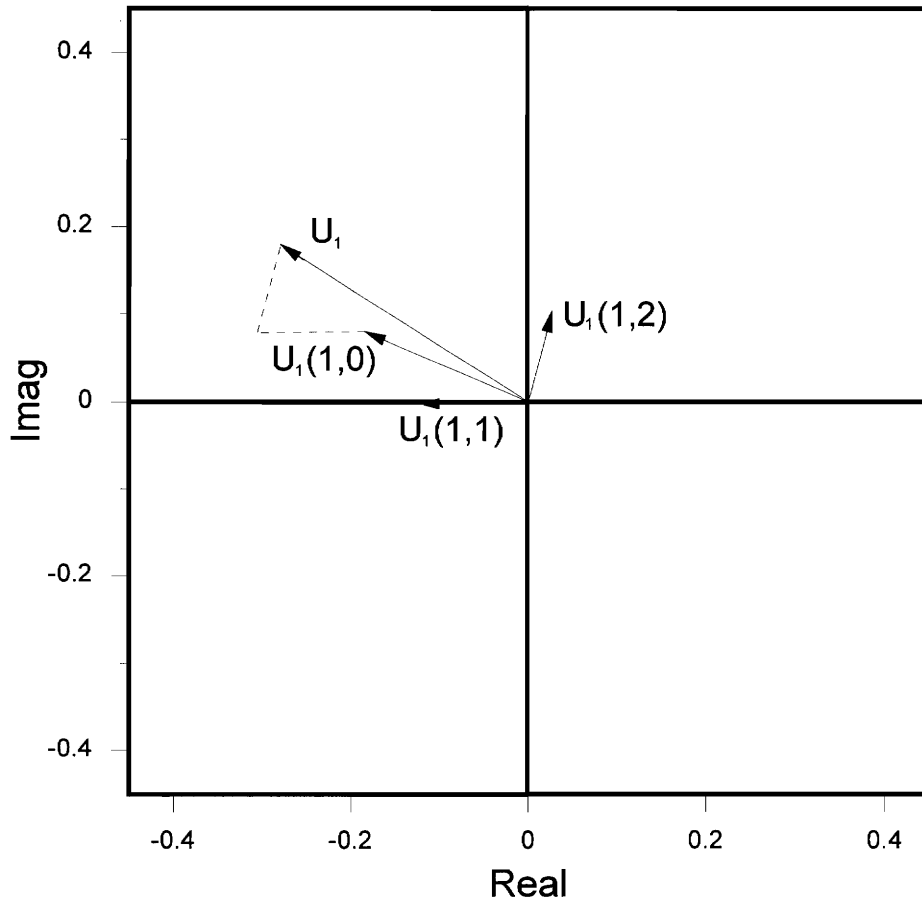
Figure 3.21. Modal breakdown of the complex control inputs for single axial control source array configuration, inlet error sensors.
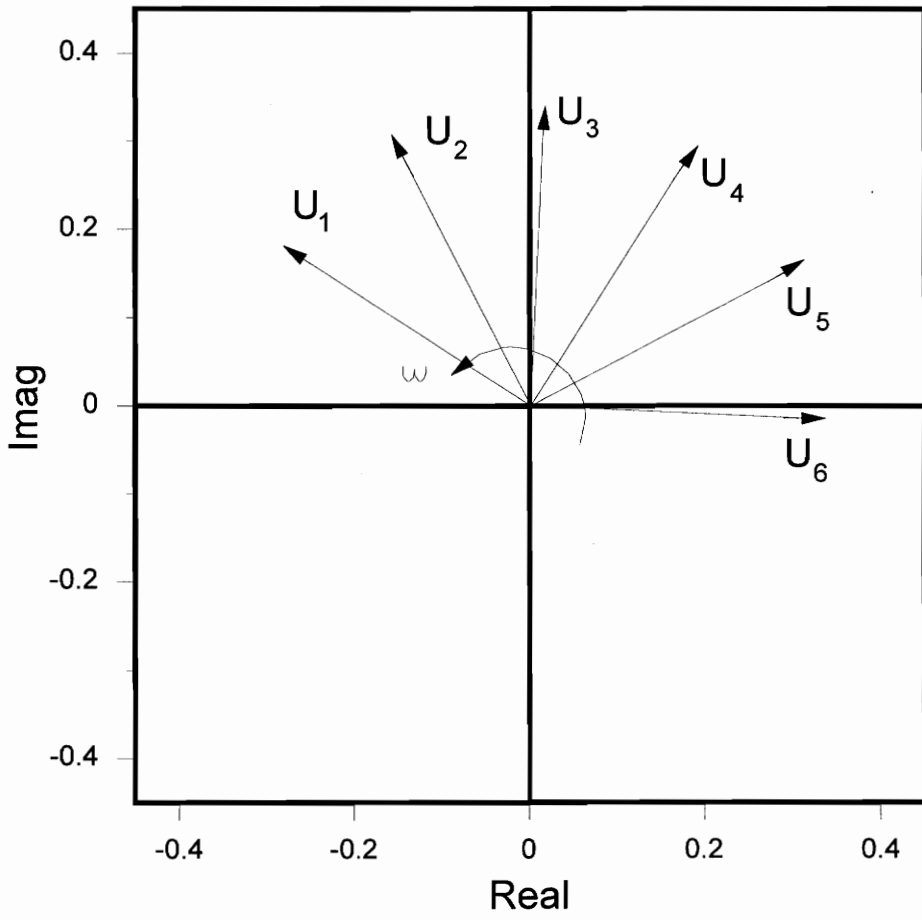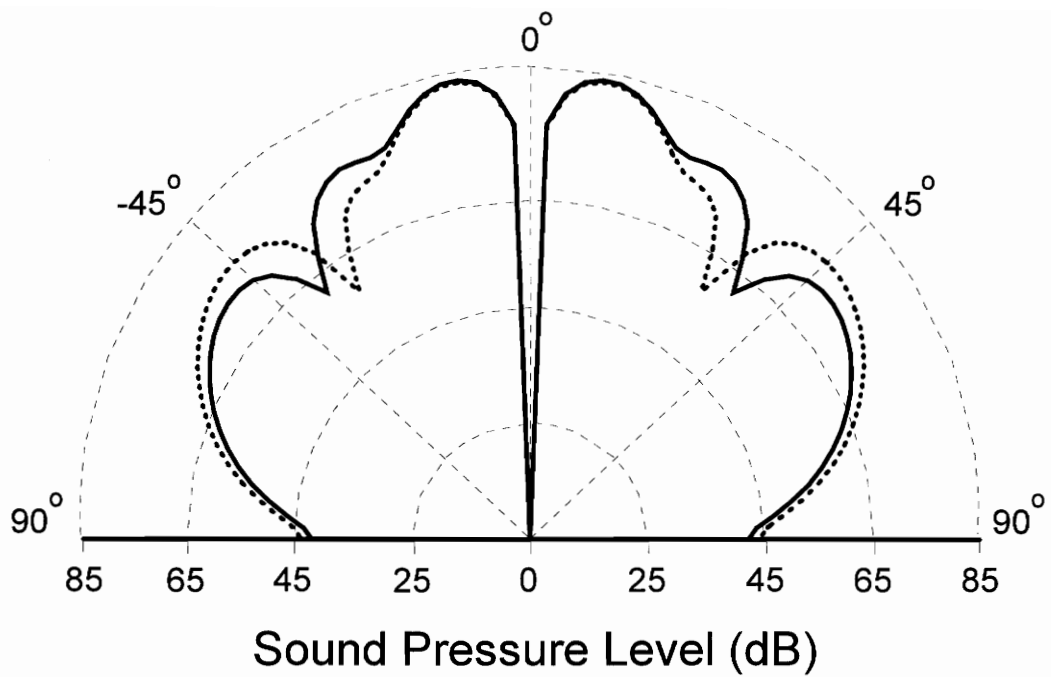
Figure 3.22. Vertical cross-section of radiation directivity for controlled fan noise using the best-case single axial control source array and inlet error sensor configuration.

3.5 Multiple Axial Array Control Configuration - Inlet Error Sensors

The potential to control the fan noise using two axial arrays of control sources and two arrays of error sensor films is now investigated. The control source band from the previous inlet sensor study, comprised of channels 1 through 6, is placed upstream of the fan. A second control source band, comprised of channels 7 through 12, is placed upstream of the first control source array and is configured similarly to the original band. Six additional error sensors are again required. These distributed sensors are of identical dimension and are placed in the same pattern about the periphery of the inlet duct as the original six. The first distributed error sensor array is placed upstream of the second control source array and the second error sensor array is placed upstream of the first error sensor array. A schematic of a generic multiple array configuration with inlet mounted sensors is shown in Figure 3.23.

The investigation for the multiple axial array configuration with inlet mounted error sensor films is again more involved. The four variables to modify in the parametric investigation are the axial location of the two control source arrays placed upstream of the fan stage and the axial locations of the two sets of error sensors, placed upstream of the control sources. For this study, the axial distance between control source stations and error sensor arrays is set and the axial location of set of control stations and error sensors is varied. Also as before, a single three-dimensional plot

73
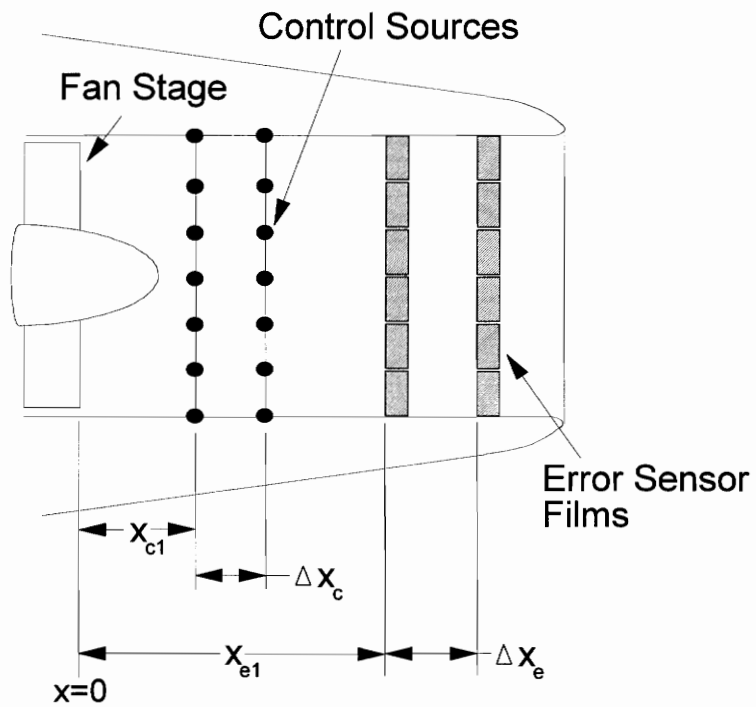
Figure 3.23. Schematic for parametric investigation, multiple axial arrays of control sources, inlet mounted distributed error sensors.

cannot display the results of four changing variables. Therefore, in this study, the locations of the first control source array and first error sensor array are specified and the second sets of each are then stepped-through to the end of the duct. Here, the distance covered by each incremental move of control sources and error sensors is greatly limited by the fact that the second set of control sources and first set of error sensors can never overlap or pass one another. Figures 3.24 through 3.26 display sample parametric study results. It is again evident in these plots that the distance relative to the sets of control source and error sensor arrays is significant. However, inspection of these figures clearly reveal peaks and valleys for a constant distance between the sets of control source and error sensor arrays, suggesting that the location of the group of arrays relative to the fan stage is also important.

The "best-case" multiple axial array configuration occurs with an axial distance between control source arrays of 0.10 m and an axial distance between error sensor stations of 0.05 m. The global attenuation results for all possible combinations of the above conditions are presented if Figure 3.24. The best performance occurs with the first control source array located 0.50 m upstream of the fan and the first distributed error sensor station placed 0.80 m upstream of the fan. The overall sound power level for this configuration is 79.96 dB, corresponding to a global attenuation of 7.60 dB. This compares to a global attenuation of 27.99 dB when controlling the fan noise with two axial arrays and far field error sensors.

The complex control inputs of this twelve channel system are presented in Figure

75

Figure 3.24. Global attenuation results for multiple control source array and inlet error sensor configuration; $\Delta x_c = 0.10$ m, $\Delta x_e = 0.05$ m.
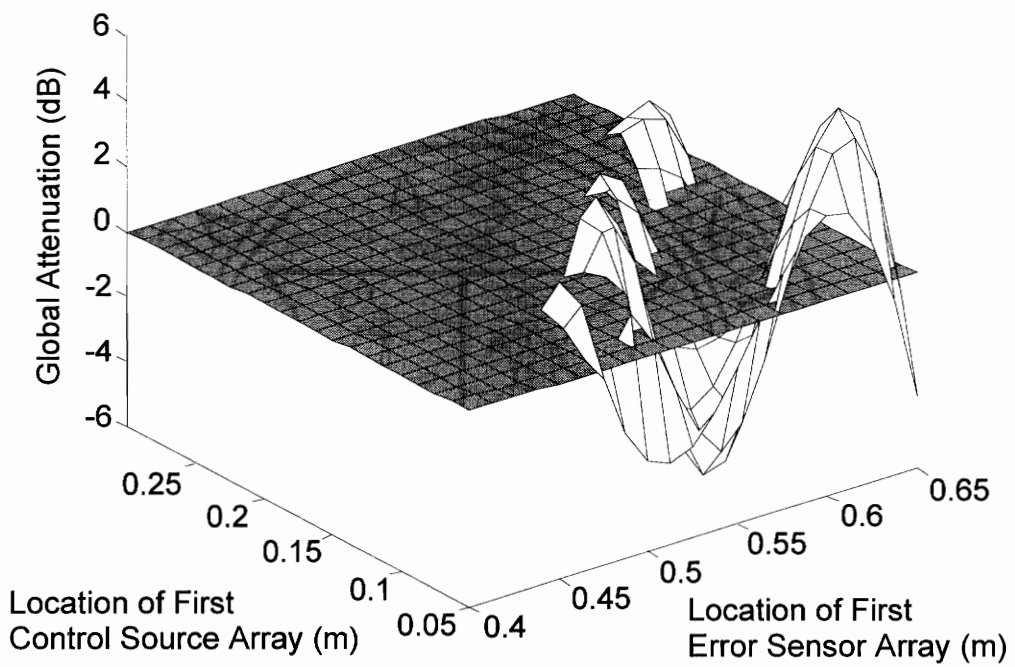
Figure 3.25. Global attenuation results for multiple control source array and inlet error sensor configuration; $\Delta x_c = 0.30$ m, $\Delta x_e = 0.25$ m.

77

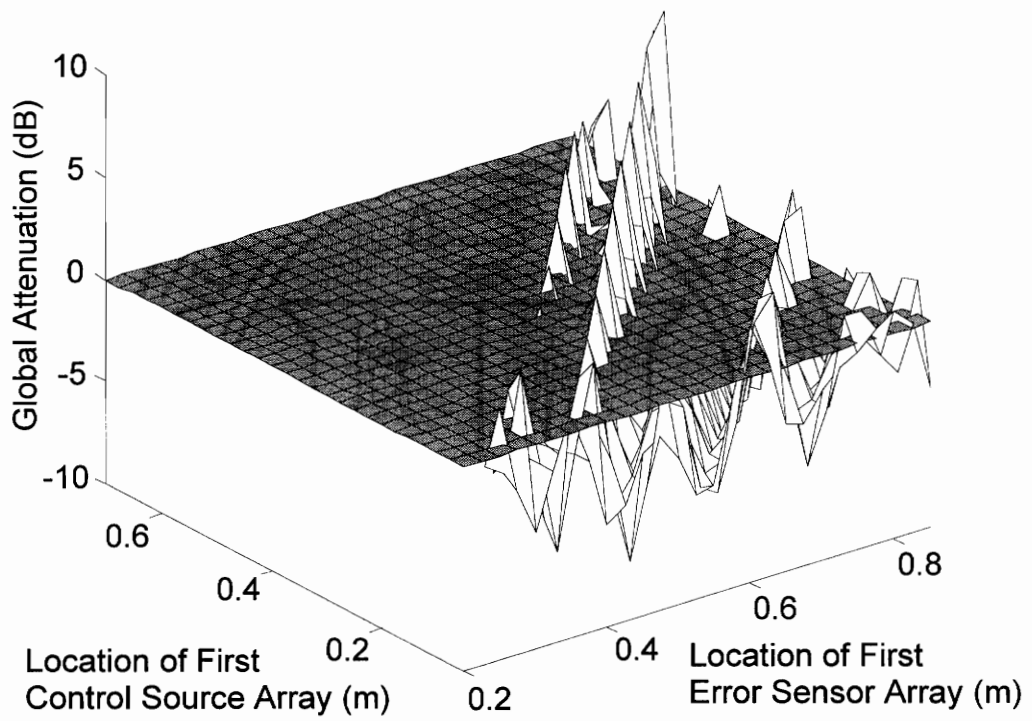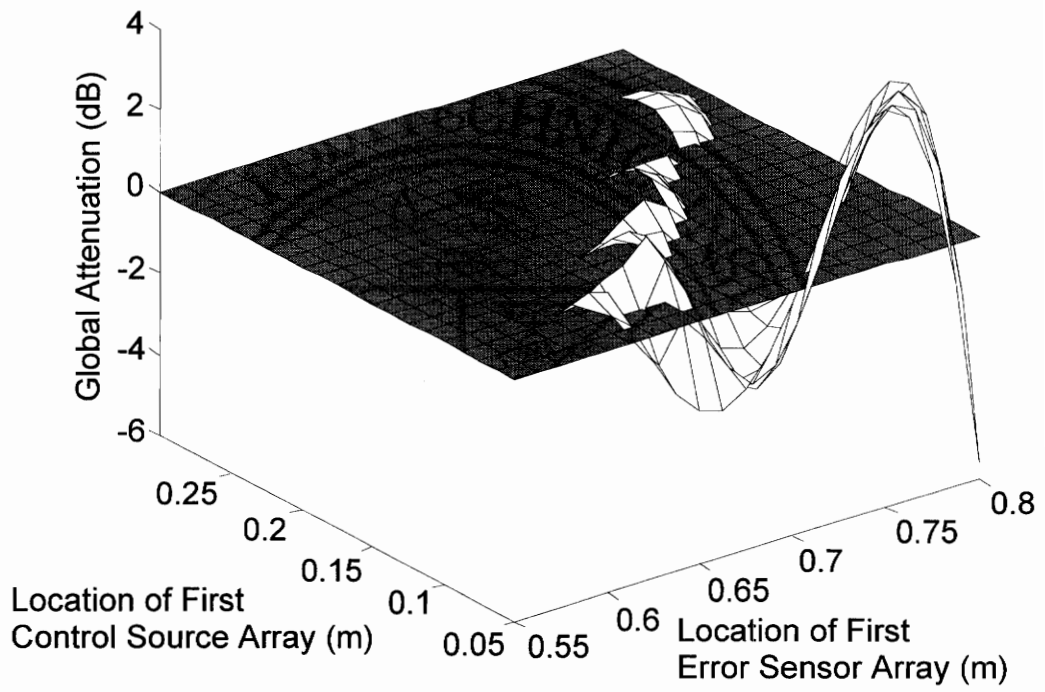Figure 3.26. Global attenuation results for multiple control source array and inlet error sensor configuration; $\Delta x_c = 0.45$ m, $\Delta x_e = 0.10$ m.

3.27. The control inputs reveal that a spinning mode pattern has been achieved by each axial station of control sources, with the magnitudes of each set differing due to the location of each band within the duct. Figure 3.28 presents the modal breakdown of the complex control inputs U_1 and U_7. It is again evident that the two axial arrays of control sources couple into the propagating fan modes with different magnitudes and phase. A vertical cross-section taken of the radiation directivity, seen in Figure 3.29, reveals that nearly global control was achieved.

The previous parametric investigations have been conducted to uncover the best possible system arrangement and to understand the mechanisms of control. For comparison purposes, the results of the four control cases are summarized. The vertical cross-section of the radiation directivities for all four best-case configurations are presented in Figure 3.30. Figure 3.30(a) and (b) compares the controlled far field radiation directivities for each sensing strategy for the configuration of single and multiple control source stations, respectively. The attenuation in sound power level and the control effort required for each best-case configuration is presented in Table II. The overall attenuation results for each configuration are measured relative to the original uncontrolled radiated fan noise of 87.56 dB. The control effort is defined as the absolute value of the complex control input, $|U_i|$
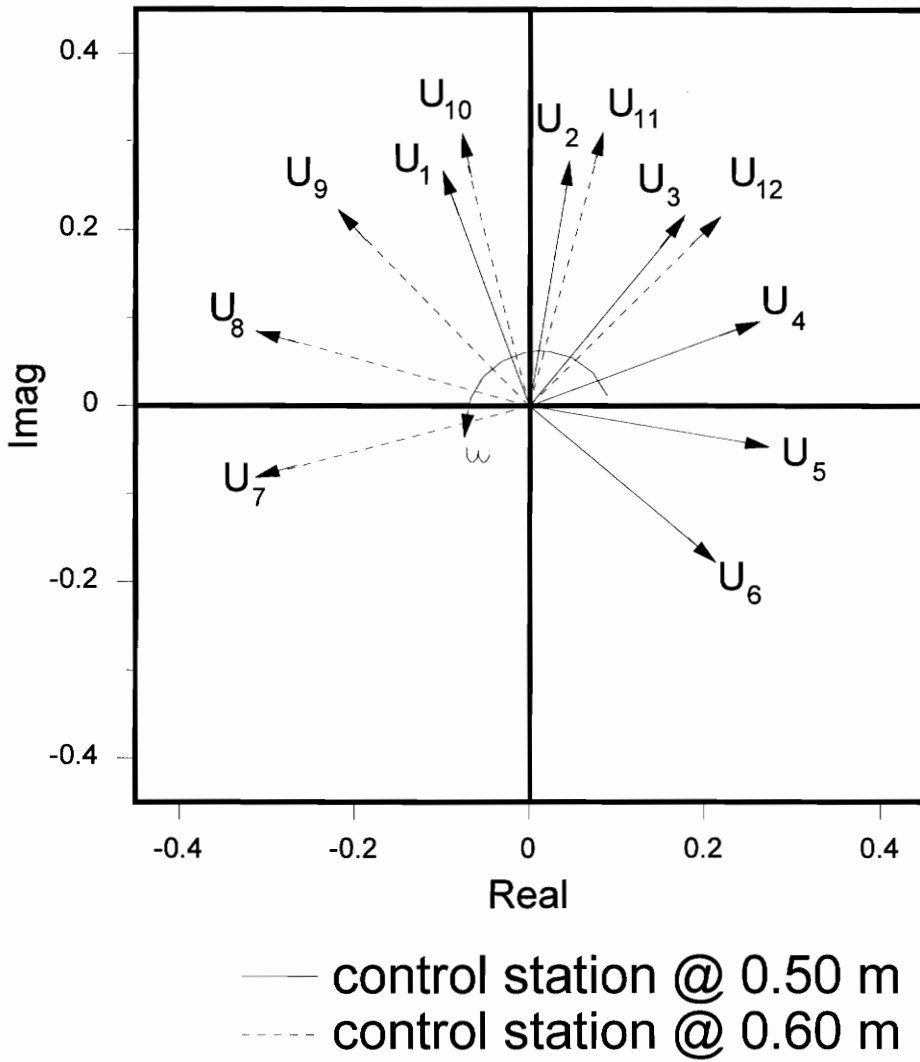
Figure 3.27. Complex control inputs for best-case multiple axial control source array and inlet error sensor configuration.
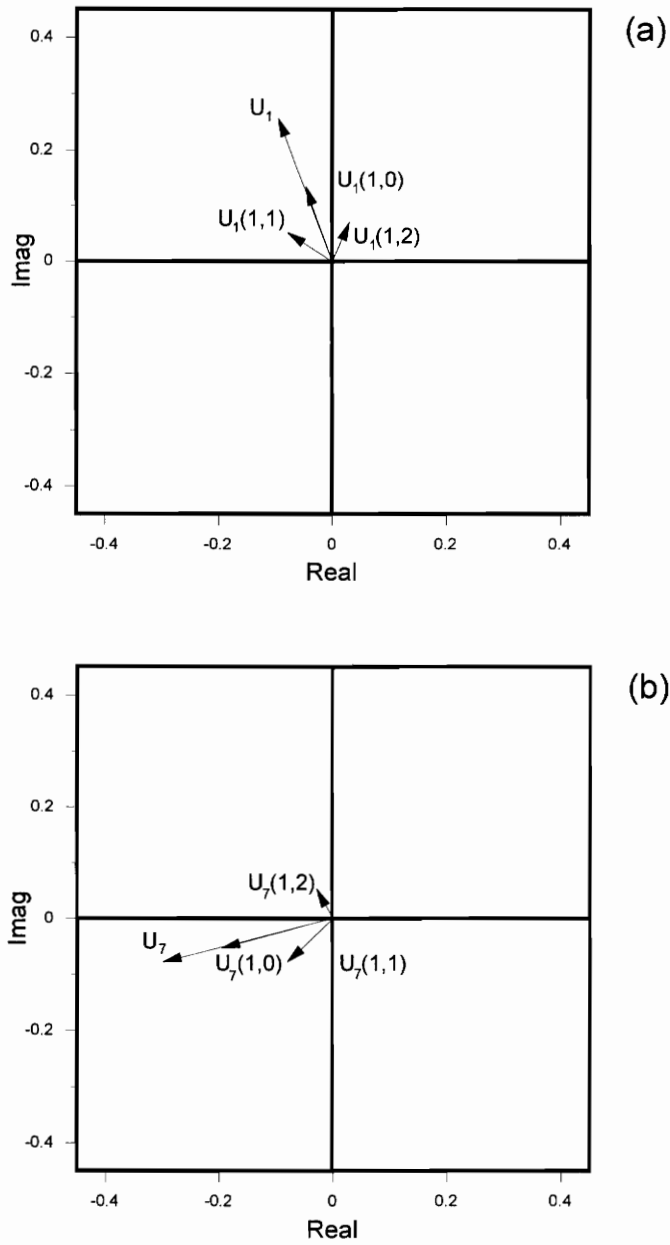
Figure 3.28. Modal breakdown of complex control inputs for multiple control source array configuration; (a) control source array at $x_{c1} = 0.50$ m and (b) control source array at $x_{c2} = 0.60$ m.
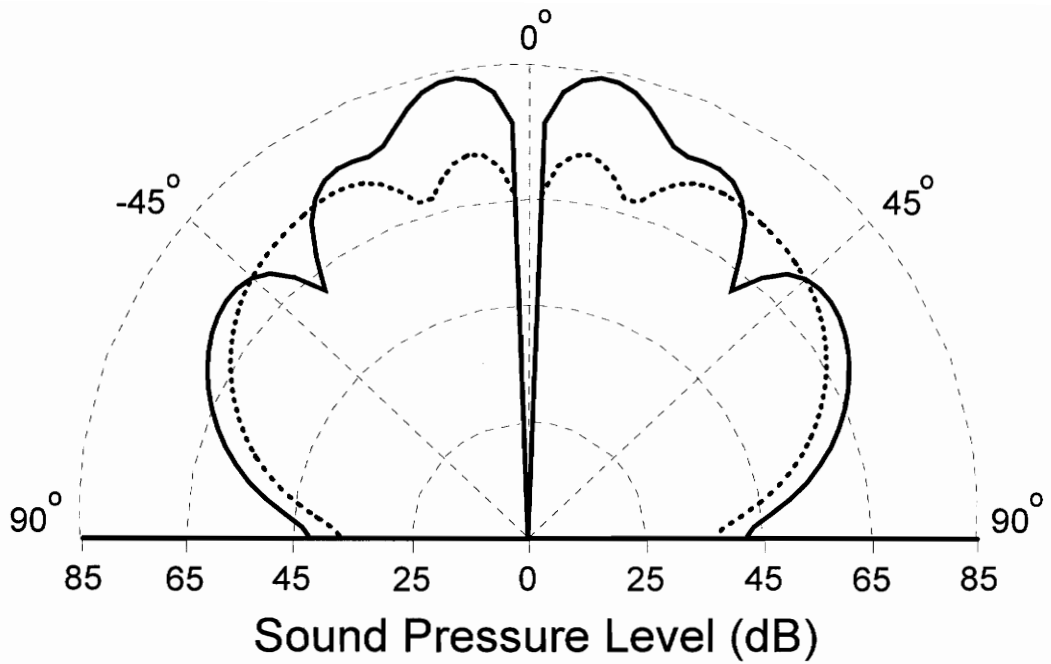
Figure 3.29. Vertical cross-section of radiation directivity for controlled fan noise using best-case multiple axial control source array and inlet error sensor configuration.
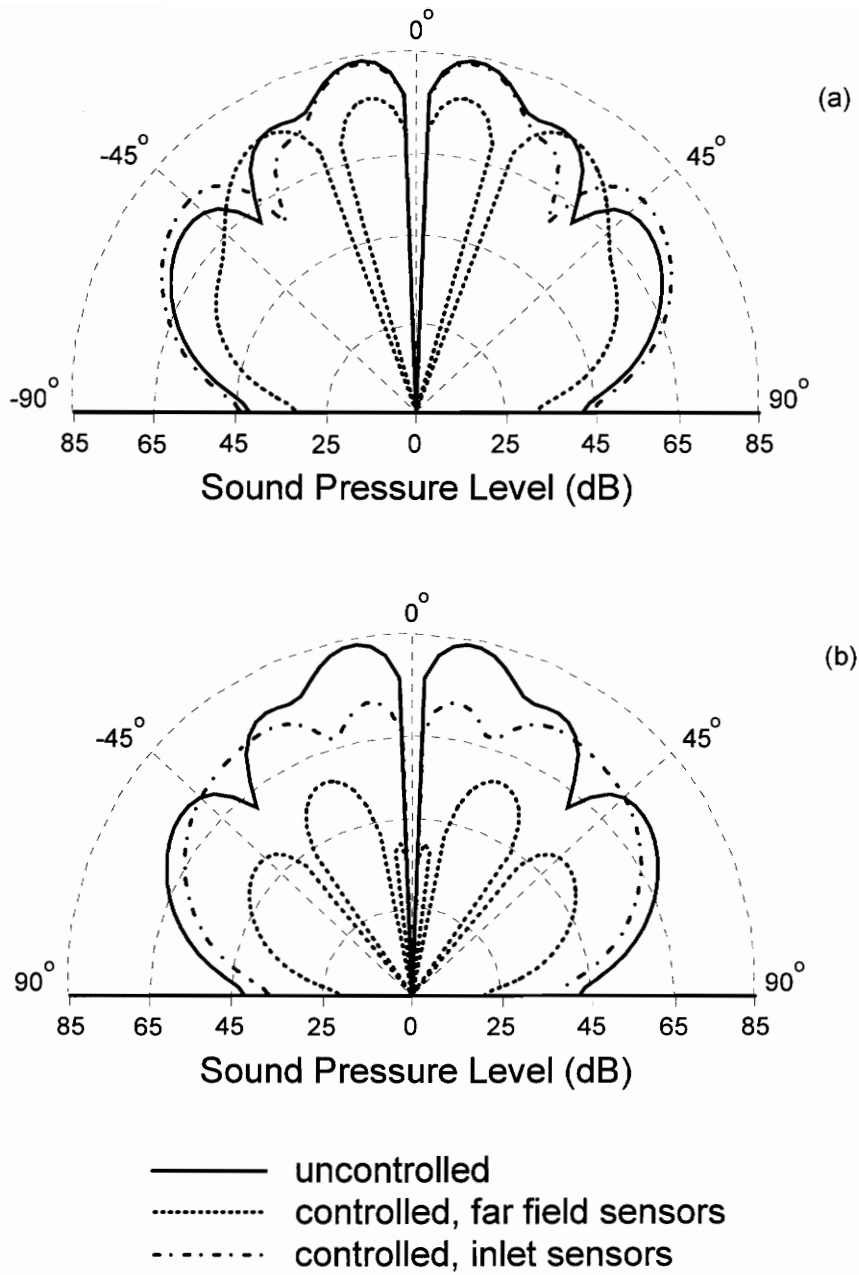
Figure 3.30. Comparison of sensing strategies for (a) single axial and (b) multiple axial control source array configurations.

Table II: Comparison of Analytical Results

System Configuration	Power Reduction (dB)	Control Effort $|U_i|$
Single Axial Control Station, Far Field Error Sensors	6.38	0.426
Multiple Axial Control Stations, Far Field Error Sensors	27.99	0.305
		0.381
Single Axial Control Station, Inlet Mounted Error Sensors	4.18	0.332
Multiple Axial Control Stations, Inlet Mounted Error Sensors	7.60	0.276
		0.307

Examination of Table II reveals that a configuration with multiple axial control source arrays and far field error sensors displays the best attenuation results with 27.99 dB.   Table II also reveals that the total control effort for the far field sensor configurations are not significantly larger than the inlet sensor cases. The larger control effort calculated for the far field sensor studies may be attributed to the fact that extra control effort is required to notch the far field radiation at the error sensors.   This additional control effort does not directly correspond to a decrease in overall sound power level. The use of far field error sensors does, however, represent an upper bound in overall sound power reduction since it directly measures the variable of interest.

It is also noted that the use of three axial stations of control sources for cases of both far field and inlet mounted error transducers was investigated. Additional error transducers were used as well. For the far field sensor scenario, a third set of six error

sensors was placed to the outside of the second error sensor sets. For the case of inlet mounted error sensors, a third band of six distributed error sensor films was added. For each system type, complete attenuation of the radiated fan noise was achieved. The three axial stations of control sources are able to couple into the three first order spinning modes generated by the engine independently. This result is analogous to the presence of three input forces controlling three modes in a structure.

3.6 Sensitivity Study

In this section, a formal effort is undertaken to understand the effect of parameter variations to the overall performance of a selected control system configuration. The far field controlled radiation and the complex control inputs of selected configurations are analyzed and an attempt is made to determine the mechanisms behind the degradation in system performance.

3.6.1 Physical Variable Modification

Here, a physical parameter of the single axial control station configuration with far field error sensors (section 3.3) is modified to determine the sensitivity of the control mechanism. The error sensor originally placed at $\beta=0°$ and $\Phi=20°$ is moved to a new angular position of $\Phi=30°$. The new position of the error sensor is 0.26 m (1.83 times the acoustic wavelength, c/f) from its previous position. All other system parameters are

maintained. The complex control inputs are presented in Figure 3.31 and show that the symmetry in the control inputs was destroyed. This implies that the total control sound field is now made up of many duct modes which do not create spinning modes. The resulting controlled three-dimensional far field radiation directivity for the modified system configuration is shown in Figure 3.32. The feature most obvious in this figure is the non-symmetrical result of this modified control scheme. The pressure distribution reveals that only localized pressure reduction is realized, occurring on or very near the error sensors, as well as areas with significant spillover effects. Figure 3.33 displays the vertical cross-section of the radiation directivity. The solid- and dotted-lines of Figure 3.33 represents the uncontrolled fan noise and controlled field, respectively. The pressure notch at the error sensor location is visible, along with a small reduction of the fan noise in the center regions. An increase in the radiated pressure, or spillover, is seen over the remaining area.

The origin of this sideline spillover is now investigated. The control system is - simulated with the modal contribution of the secondary control sources added incrementally. The fan noise is first controlled assuming the control sources excite the first order circumferential modes (m=1 and $\mu=0,1,2$). The controlled field is next computed assuming the control sources excite the first and third order circumferential modes (m=1 and 3) and finally the first, third and fifth circumferential modes (m=1, 3 and 5). The m=0, 2 and 4 order circumferential modes are not included because they are never excited by the control sources, i.e. opposite point sources driven out-of-phase.
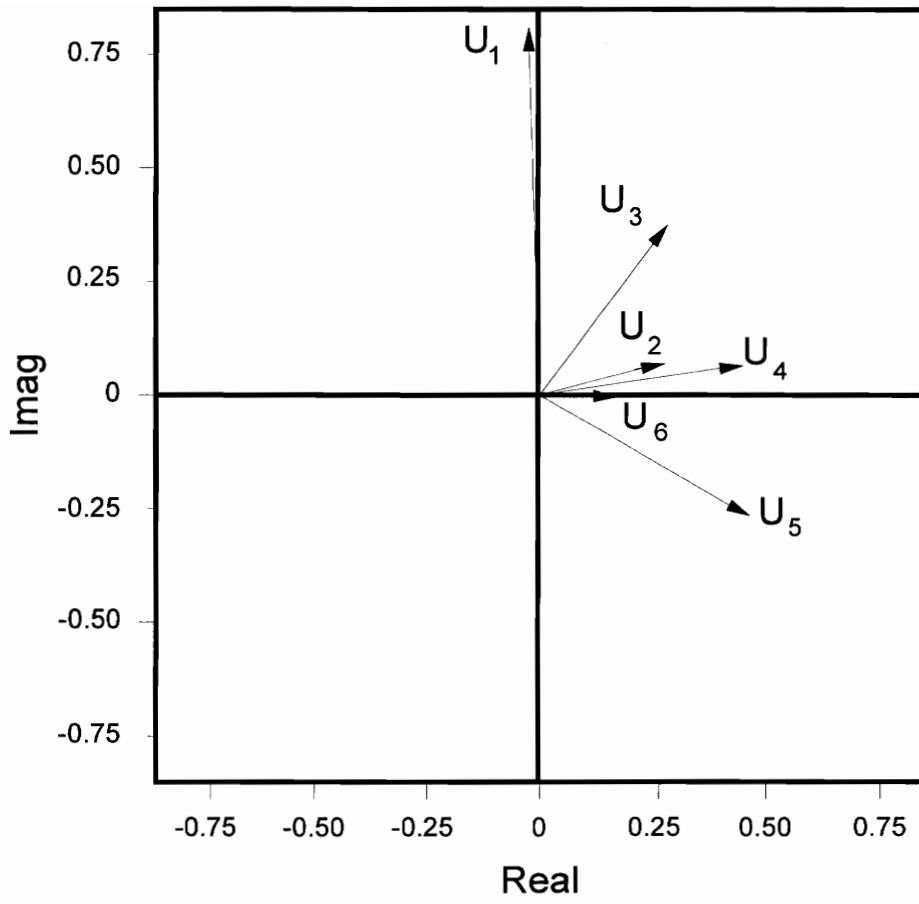
Figure 3.31. Complex control inputs for modified single axial control source configuration.
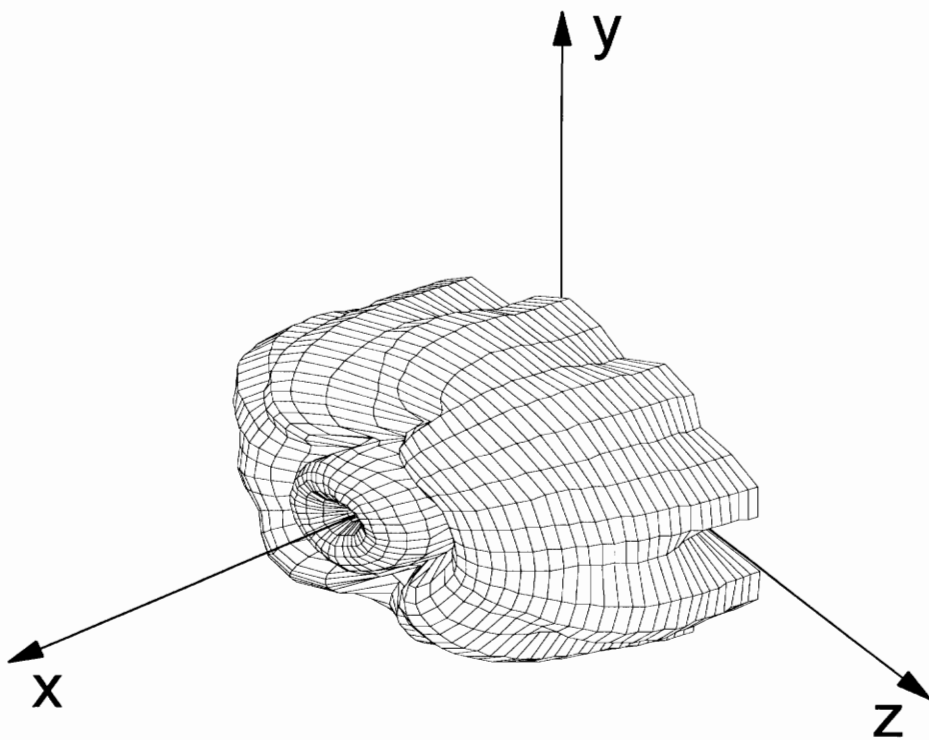
Figure 3.32. Radiation directivity of controlled fan noise using modified single axial array configuration.
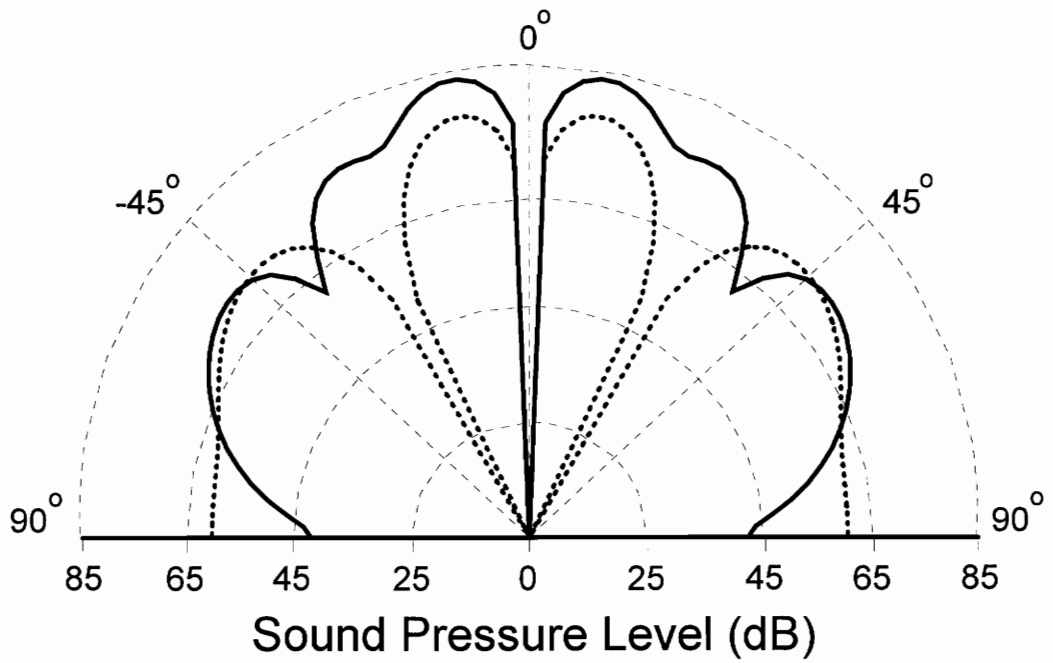
Figure 3.33. Vertical cross-section of radiation directivity for controlled fan noise using modified single axial control source configuration.

Figure 3.34 presents the vertical cross-section of the radiation directivity for the spillover investigation. It is evident from this plot that the spillover is due to the addition of the fifth order circumferential modes. To further expand the spillover investigation, the radial order modes are now added incrementally to the fifth order circumferential mode. In Figure 3.35, it can be seen that the sideline spillover is due primarily to the radial order $\mu = 1$, or more specifically, the (5,1) mode.

The previous sensitivity investigation looked at the ability of the active noise control model to adapt to a large change (10°) in the location of one error sensor. Figure 3.36 presents the control inputs and far field radiation directivities for a change in error sensor location of 1° and 3°. It is evident that the performance of the control model decreases progressively with larger displacement of the error sensor from its optimum location. The total radiated power level for each of the three modified cases of 1°, 3° and 10° is 81.34, 82.01 and 82.24 dB, respectively.

It is concluded that the location of the far field error sensors is very sensitive to the performance of the active noise control model. The movement of one error sensor relative to the sensor group induces a change in the phase for the error response. This implies that changes in the phase of the error signals due to other reasons could be very detrimental to the noise control system, i.e. phase change introduced by a signal conditioning filter.

The complex control inputs plotted in Figures 3.31 and 3.36 reveals the inefficient use of the control sources in the modified configuration. Some of the control inputs have
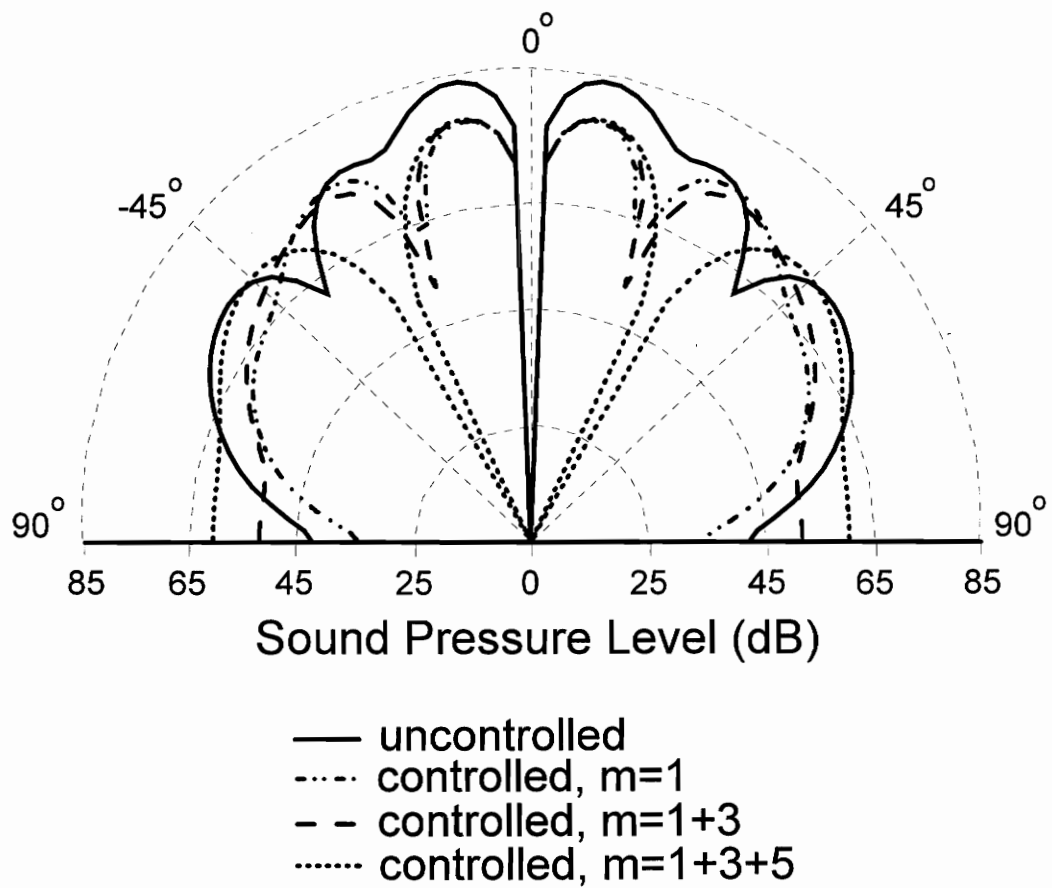
Figure 3.34. Circumferential modal breakdown for modified single axial control source configuration.
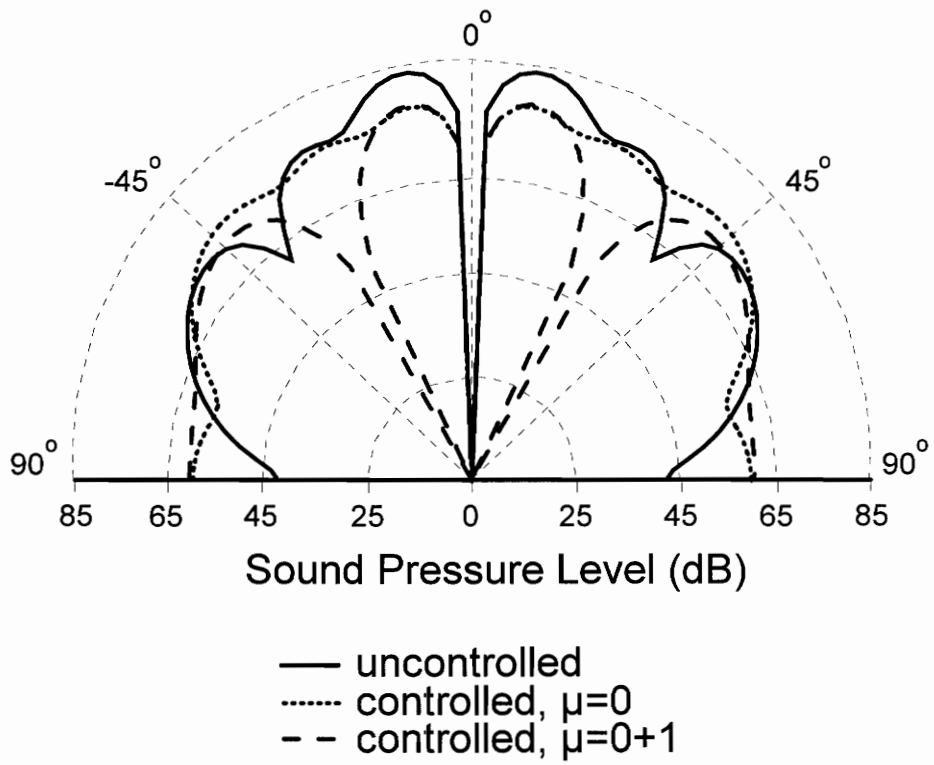
Figure 3.35. Radial mode breakdown for modified single axial control source configuration.
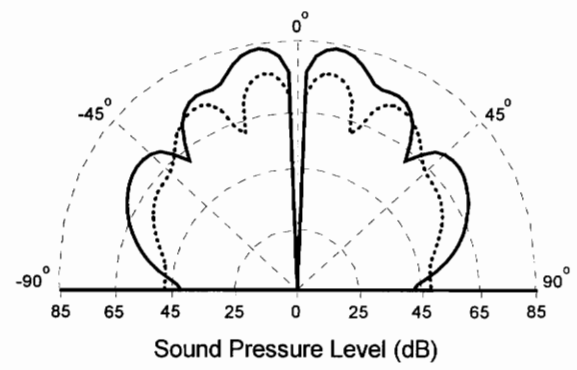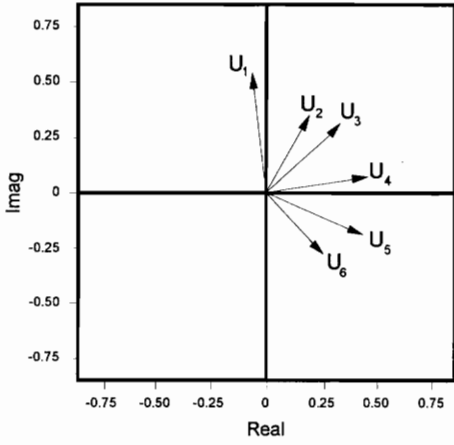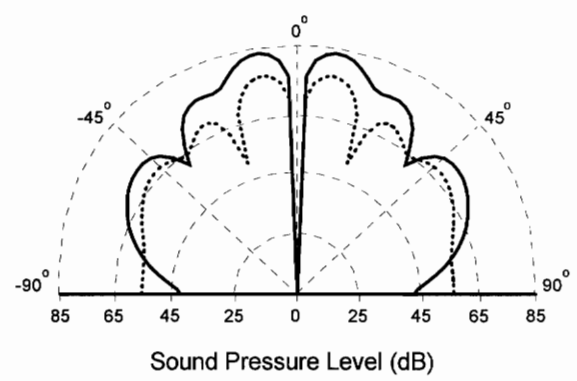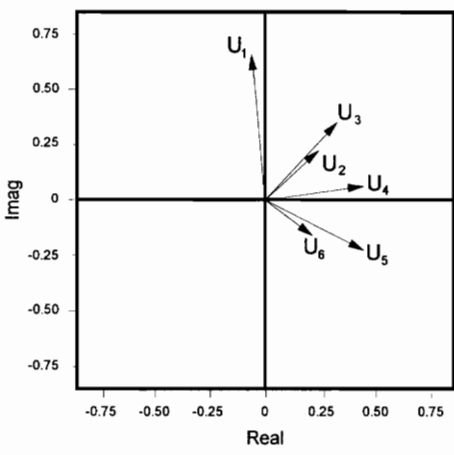
Figure 3.36. Complex control inputs and radiation directivities for modified single axial control source configuration; error sensor moved (a) 1° and (b) 3°.

93

high amplitudes, while others are driven at much lower levels. This unequal distribution of control effort results in a loss of symmetry for the problem. Although there may be instances in which an asymmetric result is desirable, retention of symmetry throughout any problem is normally advantageous.

3.6.2 Sensitivity to Acoustic Wavenumber

A study is also carried out to explore the sensitivity of the control mechanism to modifications in a parameter other than a physical constraint of the control sources and error sensors. The "best case" scenarios for the single and multiple axial array configuration using both far field and inlet mounted error sensors determined earlier are again chosen. The parameter to be modified in this sensitivity study is the acoustic wavenumber, k_o. As defined in Chapter 2, Eq.(2.2), the acoustic wavenumber is a function of the BPF, ω, and the speed of sound in air, c. Changes in either of these two variables is possible and in fact it would be common in actual applications. A variation in BPF would occur with each change in the operational condition, or speed, of the engine. If a constant speed is maintained by the engine in flight, a change in airstream temperature and/or altitude of the aircraft can result in a change in the speed of sound. Therefore, modifications in k_o will give valuable insight into the robustness of the control system in actual conditions. Figure 3.37 (a-b) presents the results of the parametric variation study. The solid lines of Figure 3.37 (a-b) represents the uncontrolled sound power of the fan, while the dotted- and dashed-lines represent the controlled sound power
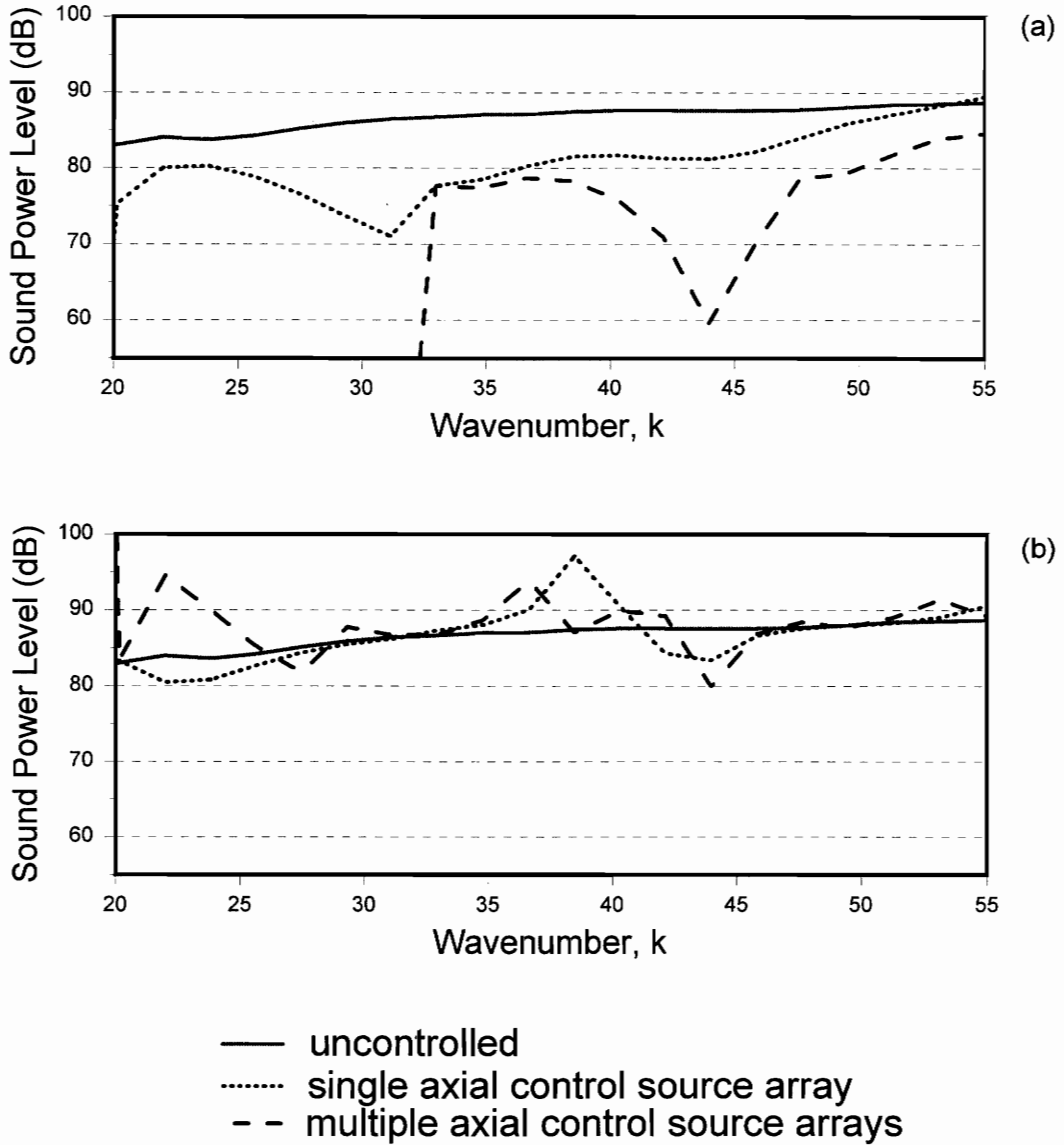
Figure 3.37. Sound power level versus acoustic wavenumber for single and multiple axial control source array configurations for (a) far field and (b) inlet error sensors.

with a single axial control station and multiple axial control stations, respectively. It can be seen that in the case of far field error sensors, the multiple control station configuration is less sensitive to a change in wavenumber than the single array case. What is of most interest in Figure 3.37(a), however, is that for each control source configuration, the far field error sensor strategies produce global attenuation in the fan noise across the variation in wavenumber. Figure 3.37(b) reveals that the inlet sensing strategies have only localized areas of global attenuation across the wavenumber variation. This implies that the inlet error sensor approach is more sensitive to changes in the original system identification.

3.6.3 Sensitivity to Mean Flow

The analytical model developed in Chapter 2 is now extended to include the effects of mean flow present in the inlet duct. The effect of mean flow is introduced into the analytical model through modifications to Eqs.(2.1) and (2.2). The pressure due to the fan disturbance given by Eq.(2.1) is redefined as [19]

$$(P_i)_d = \sum_{m,\mu} A_{m\mu} J_m(k_{m\mu} r) e^{-im\theta} e^{-i(k_x x + k_d M x) / \mu^2} \tag{3.2}$$

and where the axial wavenumber k_x, is now defined as

$$k_x = \sqrt{k_o{}^2 - (1-M^2)\, k_{m\mu}^2}$$ (3.3)

where $\mu = (1-M)^{\frac{1}{2}}$ and M is the axial flow Mach number.

Investigation of Eq.(3.3) reveals that the addition of mean flow effects the cut-on condition of the modes at a given BPF. A mode is cut-on and propagates along the duct for real values of k_x, i.e. $k_o{}^2 \geq (1-M^2)k_{m\mu}{}^2$. The effect of mean flow in the duct is in the alteration of the modal cut-on frequencies and the axial wavenumber. Table III lists the value of the axial wavenumber, k_x, for the condition of no mean flow (M=0) and for Mach numbers of 0.2 and 0.5 for each possible mode index at a BPF of 2400 Hz. It can be seen, for example, that for Mach numbers of 0 and 0.2, the (0,4) mode pattern is cut-off. However, at a Mach number of 0.5 the (0,4) mode does propagate. Figure 3.38 (a-c) presents the vertical cross-section of the far field radiation directivity for a single axial control source array configuration with no flow present and with flow of M=0.2 and M=0.5, respectively. The solid and dashed-lines of Figure 3.38 (a-c) represents the two-dimensional uncontrolled fan noise and controlled far field radiation directivity, respectively. The system configuration used for this study was the best-case single axial control source station configuration using far field error sensors as described earlier in this chapter. The controlled total radiated sound power in these figures are 81.18, 81.89 and 88.46 dB, respectively.

Figures 3.38(a) and (b) exhibit nearly global control of the radiated fan noise. Figure 3.38(b), however, reveals that considerable sideline spillover has been generated

Table III: Wave Number Variations with Mean Flow Present in Inlet Duct

Modal Index (m,μ)	Flow Mach Number		
	0.0	0.2	0.5
0,0	43.96	43.96	43.96
0,1	41.52	41.62	42.14
0,2	35.09	35.49	37.50
0,3	21.45	22.78	28.78
0,4	0.0	0.0	6.16
1,0	43.41	43.43	43.55
1,1	39.09	39.30	40.37
1,2	29.90	30.59	33.97
1,3	**0.0**	**7.64**	**21.64**
1,4	0.0	0.0	0.0
2,0	42.43	42.49	42.82
2,1	35.94	36.30	38.10
2,2	22.75	23.96	29.52
2,3	0.0	0.0	8.97
2,4	0.0	0.0	0.0
3,0	41.01	41.13	41.77
3,1	31.89	32.46	35.30
3,2	9.92	13.11	23.60
3,3	0.0	0.0	0.0
3,4	0.0	0.0	0.0
4,0	39.11	39.32	40.38
4,1	26.58	27.49	31.83
4,2	0.0	0.0	14.69
4,3	0.0	0.0	0.0
4,4	0.0	0.0	0.0
5,0	36.71	37.03	38.65
5,1	18.89	20.49	27.40
5,2	0.0	0.0	0.0
5,3	0.0	0.0	0.0
5,4	0.0	0.0	0.0
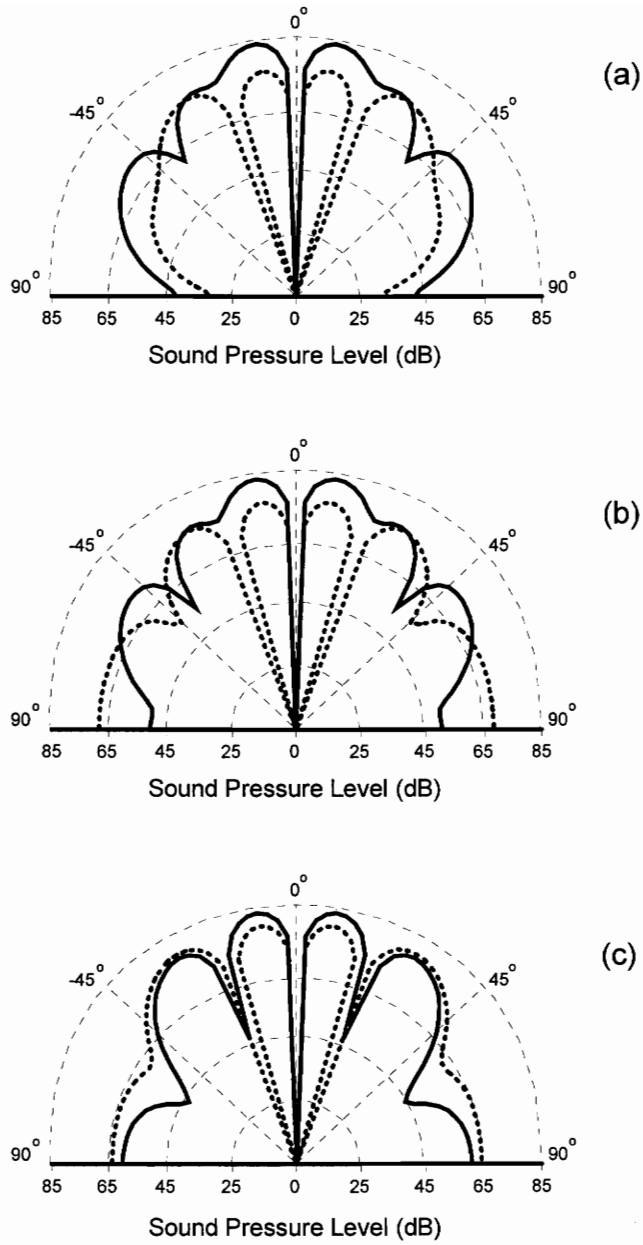
Figure 3.38. Vertical cross-section of far field radiation directivity for a single axial control source array configuration with the effect of mean flow; (a) M=0.0, (b) M=0.2, (c) M=0.5.

99

with a mean flow of M=0.2. This can be understood by revisiting Table III. It can be seen from Table III that with flow Mach numbers of 0.2 and 0.5, the (1,3) mode is excited and will propagate. Closer examination reveals that the (1,3) mode is just above cut-on for M=0.2. A mode just above the cut-on frequency will radiate towards the sidelines. This is seen as sideline spillover in Figure 3.38(b). Figure 3.38(c) reveals less sideline spillover because the (1,3) mode is well cut-on for M=0.5. An increase in sound pressure level in the areas away from the error sensors is also observed that results in a net increase of radiated power. The poor performance of the control system is due to the presence of an additional mode, i.e. (1,3), strongly radiating in the direction of the error sensors. Thus, the results of the mean flow study suggests that a mode near its cut-on frequency will be difficult to attenuate with an active control system. These low wavenumber modes, however, can be effectively cancelled with passive control methods, i.e. duct liners.

3.7 Principle Component Analysis

The work in this chapter compares the analytical approach developed in Chapter 2, to a statistical technique, referred to as principle component analysis (PCA) [18], applied to the reduction of fan noise. PCA has proven successful in determining the optimum inputs to the control sources of an active control system, even if the control problem is ill-configured. PCA also provides insight into the mechanisms of active control by breaking the action of the control actuators into a set of orthogonal

components. The action of the control system can then be clearly understood as the summation of non-interacting components. PCA is useful for discovering hidden relationships between input and output data, and for dealing with extraneous degrees of freedom in a model. For an active noise control system, this implies that the influence of a large number of actuators can be reduced to a smaller number of principle components.

For the PCA approach applied to the fan noise problem, a model was created consisting of one or more arrays of secondary control sources and a large array of far field error sensors. Each axial array of control sources is configured as twelve evenly distributed point sources placed along the periphery of the inlet duct. For the PCA study, however, the control channels are not forcibly specified. Instead, the PCA approach is used to determine the optimal complex control input for each control source that will produce the greatest attenuation of the fan noise. The far field error sensors used in this approach consists of 276 point error sensors distributed evenly about a hypothetical hemisphere of radius 1.5 m placed in front of the duct opening. This is equivalent to minimizing the total radiated power. The use of 276 microphones is obviously unrealistic form a practical standpoint, but control source optimization is the goal of the PCA work as opposed to sensor optimization. The results of the PCA approach are absolute "best-case" scenarios for each axial position of the control source array(s).

The actuator, or control source, inputs obtained from the PCA approach revealed

results similar to the configuration used in the modal approach which was devised from physical considerations of the problem. In the PCA approach, each actuator is driven with signals of the same amplitude and with actuators opposite one another in the duct driven 180° out-of-phase. The resulting control noise field couples into the first order spinning modes of the disturbance noise field.

Figure 3.39 presents the global attenuation results for a single axial array of control sources for both the PCA and modal approaches as a function of the axial location. The solid line of Figure 3.39 represents the global attenuation achieved with the PCA approach. The dotted-line represents the *optimum* results obtained from the modal approach. In this approach, six microphones (placed as shown in Figure 3.5 are used as error sensors. The angular position of the error sensors, Φ, is optimized for each axial location of the control sources. For instance, the best system performance of the modal approach with a single array of control sources located 0.2 m upstream of the fan corresponds to $\Phi=20°$ off the engine centerline axis, as described in Section 3. The optimum angle Φ of the error sensors for each control source location is indicated in the figure in parenthesis if it is something other than $\Phi=20°$. It is clear that the modal approach out-performs the PCA approach.

The dashed-line of Figure 3.39 represents the performance of the modal approach for a constant angular position of the far field error sensors, which in this case is 20°. It is seen that this angular position of the error sensors corresponds to the best-overall performance of the modal approach for nearly all control source locations up to 0.65 m

102
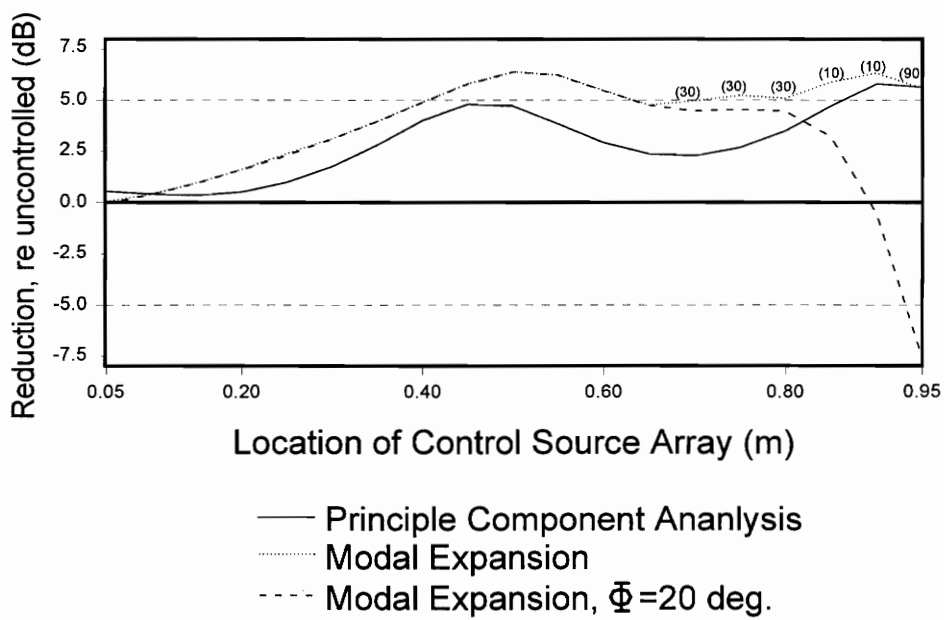
Figure 3.39. Global attenuation versus control source array location for modal and principle component analysis approaches.

from the fan stage. For control source positions greater than 0.65 m from the fan, the system performance drops rapidly with the 20° error sensor position maintained.

Figure 3.40 presents the complex control inputs obtained with each analytical method for a location of control sources of $x_c = 0.5$ m. For each approach the control inputs display equal magnitude and an equal phase angle between consecutive inputs corresponding to the angular position of each control source, in the case of the PCA approach, or the angular separation of the control channels in the case of the modal approach. The greater control effort, or magnitude of the control inputs, of the modal approach is evident in Figure 3.40. Figure 3.41 presents the magnitude of the complex control inputs as a function of control source location for the PCA and modal approaches. For each axial position of the control source array, the control effort required to obtain nearly similar attenuation results is greater for the modal approach.

Figure 3.40. Complex control inputs for analytical comparison of (a) modal approach and (b) principle component analysis approach.

105

Figure 3.41. Comparison of magnitude of complex control inputs for modal and principle component approaches.
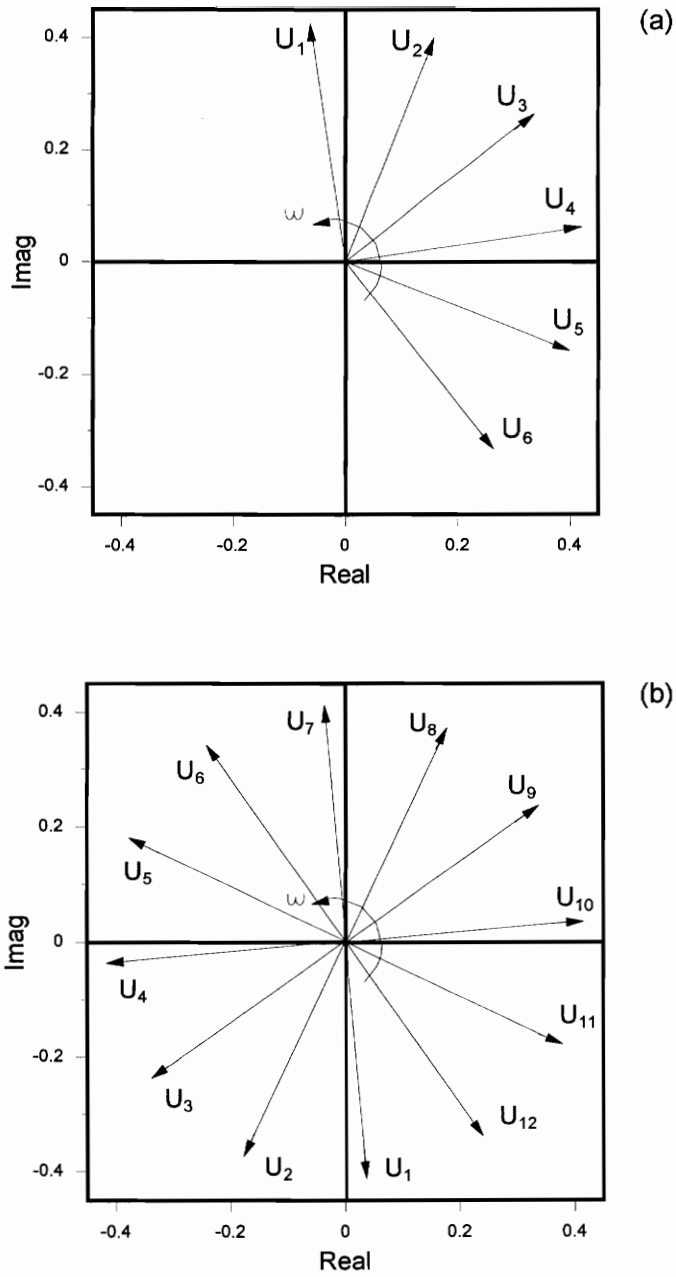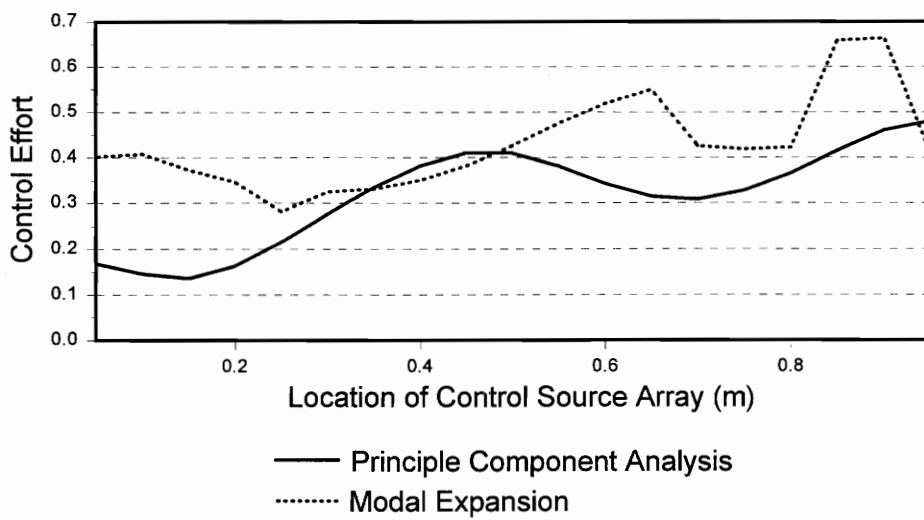
Chapter 4

Conclusions and Recommendations

4.1 Conclusions

An analytical model has been developed and its validity verified which can predict the resulting far field radiation from a turbofan engine inlet. A feedforward control algorithm was simulated to predict the controlled far field radiation from the destructive combination of fan noise and secondary control sources. The analytical model developed in this work was used to investigate the potential of active noise control in reducing tonal inlet noise radiated from turbofan engines. The main objective of this work was to identify the basic control mechanisms which govern the performance of an active control system in reducing the undesired noise. For the purposes of analytical investigation, a Pratt and Whitney JT15D turbofan engine was modeled and different configurations of secondary control sources and error transducers were tested. System configurations included single and multiple arrays of control sources and far field point and inlet mounted distributed error transducers. Results of the analytical model were compared to experimental results obtained at Virginia Tech.

A complex analytical model was not required at this stage of the investigation. The analytical model described in this work contains the basic components of an active control system, i.e. error sensors, control channels and so forth, without the complexity

107

required to accurately describe a turbomachine source.

A parametric study was conducted using the analytical model to determine the best overall control system configurations for different control source and error sensor specifications. The "best-case" configurations for single and multiple axial arrays of secondary control sources using error transducers placed either in the acoustic far field or within the inlet duct itself were identified and numerical results were generated to observe the structure of the complex control inputs and controlled far field radiation. It was demonstrated that reduction in overall sound power of nearly 28 dB of the fan noise is possible with multiple control source arrays and far field error sensors. The addition of a second control source array placed at a different axial location enables the control source to couple into the various radial modes of the fan disturbance. The results show that significant degradation in control performance is observed when inlet sensors are used.

A formal sensitivity analysis was conducted to address the effect of modified model parameters on the overall system performance for single and multiple control source array configurations. The resulting controlled far field radiation patterns of selected cases showed varying degrees of attenuation and spillover. With one axial station of control sources and far field error sensors with equal relative angular positions, nearly global attenuation is achieved. However, the performance of the control system was found to be sensitive to changes in control parameters, i.e. modified error sensor locations resulted in an increase of spillover to the sidelines with a net increase in

radiated power. The origin of this sideline spillover was due to the excitation of higher order modes by the control source.

The sensitivity analysis also included the effect of changes in the acoustic wavenumber, k_0, on overall reduction of the far field radiated noise. It was observed that systems with far field error sensors and either single or multiple control source arrays were able to attenuate the far field sound power throughout a range of wavenumber values. The system configurations using inlet error sensors, however, revealed only localized areas of attenuation with the same range of acoustic wavenumbers.

The analytical model was extended to include the effects of mean flow present within the inlet duct. It was shown that the inclusion of mean flow caused more modes to be cut-on, or present, within the duct. This scenario affected the ability of the control system to attenuate the far field sound pressure towards the sidelines. The cause of the system shortcoming was identified and explained.

Finally, the operation of the analytical model was then compared to the work of an outside investigator. In a similar analytical attempt to control the far field radiation of a turbofan engine using a principle component analysis approach, the results of the modal approach presented in this work were found to match the PCA results closely.

In summary, the analytical work presented here demonstrates that active noise control of tonal inlet noise is feasible. However, the attenuation of the far field radiation depends on a critical combination of control source and error sensor placement. It was

demonstrated that a control system using far field error sensors and multiple control source arrays results in significant global attenuation of the far field radiation. System using inlet mounted error sensors results in a net attenuation of the far field radiation, yet the controlled radiation directivity exhibits spillover of acoustic energy in some areas. The use of an inlet error sensor strategy has potential to attenuate the far field sound pressure radiated from a turbofan source, although more research is needed in the areas of sensor and transfer function design.

4.2 Recommendations

The recommendations for future work include extending the model to consider the effects of acoustical reflection at the fan and at inlet opening. These reflections will generate standing patterns that can have a profound effect on the control system. The effect of non-propagating or evanescent modes to the performance of the active control system should also be included. Experimental results from the team at Virginia Tech have shown more sound pressure energy at the extreme sidelines than that seen in the analytical results. This radiation to the sidelines may be attributed to the existence of evanescent modes that exit the inlet duct at wide angles to the duct centerline axis. Thus, inclusion of these modes will more closely match the experimental setup.

The analytical model can also be extended to investigate the potential of using a passive/active hybrid noise control system. Attenuation of the fan noise could be

attempted with an active control approach to attenuate the modes which are well cut-on while a passive duct liner could be used to attenuate the modes just above cut-on and the evanescent modes.

Control of multiple tones, i.e. BPF and harmonics, should be investigated. Simultaneous control of multiple tones was demonstrated experimentally by the team at Virginia Tech and the model could be used to uncover the mechanics behind this control approach.

Finally, the model can be used to investigate different types and shapes of control sources. For instance, a control source could be defined with dimensions to imitate the electromagnetic horns used in the experimental work at Virginia Tech. The goal here is to determine the performance of the active control system with real world limitations. The actual implementation of an active control system on a turbomachine source depends heavily on the design of compact, lightweight and electrically efficient actuators.

To conclude, the analytical model is an ideal platform to study the problems encountered in actual applications of active tonal inlet noise control. Items such as control source limitations, error sensor placement and the presence of multiple tones in actual systems present substantial problems for the acoustical engineer.

Bibliography

1. Peterson, John E., *Airports for Jets,* Blakely-Oswald Printing Company, 1959.

2. Leug, Paul, "Process of silencing sound oscillations," US patent 2.043.416, 1934.

3. Thomas, R.H., Burdisso, R.A., Fuller, C.R., and O'Brien, W.F., "Active Control of Fan Noise from a Turbofan Engine," AIAA 93-0597, January 1993.

4. Thomas, R.H., Burdisso, R.A., Fuller, C.R., and O'Brien, W.F., "Preliminary Experiments on Active Control of Fan Noise from a Turbofan Engine," *Journal of Sound and Vibration*, 161(3), 532-537, 1993.

5. Burdisso, R.A., Thomas, R.H., Fuller, C.R., and O'Brien, W.F., "Active Control of Spinning Acoustic Modes from a Turbofan Engine," AIAA 94-0361, January 1994.

6. Kroft,R.E., Kontos,K.B., "Theoretical Implications of Active Noise Control for Turbofan Engines," AIAA 93-4355, October 1993.

7. Berge, D., Bouty, E., and Cailleau, J.M., "Active Noise Control of a Jet Engine at Low Frequency Radiation: B.E.M. for Predicting Far-Field Noise Radiation," AIAA 93-4354, October 1993.

8. Fleeter, Sanford, "Active Control of Turbomachine Discrete Tones," Proceedings of Noise-Con 94, pp 379-388, 1994.

9. Tyler, J.M., and Sofrin, T.G.,"Axial Flow Compressor Noise Studies," SAE Transaction no. 70, pp. 309-332, 1962.

10. Kinsler, L.E., Frey, A.R., Coppens, A.B., and Sanders, J.V., *Fundamentals of Acoustics*, Wiley, 1982.

11. Morse, P.M., and Ingard, K.U., *Theoretical Acoustics*, University Press, 1986.

12. Morfey, C.L., "A Note on the Radiation Efficiency of Acoustic Duct Modes," *Journal of Sound and Vibration,* 9(3), 1969, pp. 367-372.

13. Fahy, F., *Sound and Structural Vibration*, Academic Press, 1989.

14. McLachlan, N.W., *Bessel Functions for Engineers*, Oxford, 1934.

15. Greville, T.N., "Some applications of the pseudo-inverse of a matrix," SIAM Review, Vol. 2, No. 1, 1960, pp. 15-37.

16. Clark, Robert L., "Advanced Sensing Techniques for Active Structural Acoustic Control," Doctoral Dissertation, Virginia Tech, 1992.

17. Anderson, Gregory L., "The Development of poly (vinylidene fluoride) piezoelectric sensors for measuring peel stresses in adhesive joints," Masters Thesis, Virginia Tech, 1992.

18. Cabell, R.H., Risi, J.D., Burdisso, R.A., and Fuller, C.R., "Principle Component Analysis for Active Control of Turbofan Noise," a research note from NASA Langley Research Center, Hampton, Virginia, December, 1994.

19 Goldstein, Marvin E., *Aeroacoustics*, McGraw Hill, Inc., 1976.

Appendix A

The secondary control sources, modeled as point sources in the analytical model of Chapter 2, are assumed embedded in the duct wall of the engine inlet. The control sources are assumed to excite all possible modes from the plane wave (0,0) to the fifth order spinning mode with radial components (5,4). The modes allowed to propagate along the duct are governed by the cut-off frequency, as described in section 2.1. The magnitude of the (m,μ) modes excited by one point source is termed here as the modal influence factor, $f_{m\mu}$. The modal influence factor is derived from the Green's function for a positive-x traveling wave, Eq.(2.4):

$$(P_i)_c^n(r,\theta,x) = \frac{-i}{2\pi a^2}\sum_{m\mu} \frac{\Psi_{m\mu}(r,\theta)\ \Psi_{m\mu}(a,\theta_n)}{\Lambda_{m\mu}\ k_x}\ e^{-ik_x|x_i-x_n|} \tag{2.4}$$

where $\Psi_{m\mu}(r,\theta)$ and $\Lambda_{m\mu}$ are defined in Eqs.(2.5) and (2.6), respectively. The terms in Eq.(2.4) that are dependent on modal index numbers (m,μ) are separated and the modal influence factor is defined as

$$f_{m\mu}(r,\theta,x) = \frac{\Psi_{m\mu}(r,\theta)\ \Psi_{m\mu}(a,\theta_n)}{\Lambda_{m\mu}\ k_x} \tag{A.1}$$

where the propagating exponential term has been omitted because its magnitude is unity. Substituting Eqs.(2.5) and (2.6) in Eq.(A.1) yields

$$f_{m\mu}(r,\theta,x) = \frac{\cos(m(\theta - \theta_n)) \, J_m(k_{m\mu}r) \, J_m(k_{m\mu}a)}{\frac{k_x}{\varepsilon_m}\left[1 - \frac{m^2}{(k_{m\mu}a)^2}\right] J_m^2(k_{m\mu}a)} \tag{A.2}$$

Eq.(A.2) indicates that the modal influence factor, at a point (r,θ) within the duct, is a direct measurement of the relative contribution of each mode excited by a point control source. For example, arbitrarily selecting a point source at $(a, \theta_n =)$ and an observation point in the duct of $(a, \theta = 0°)$, the modal influence factors are presented in Figure A.1 for a fan BPF of 2400 Hz. The modes which propagate at the BPF are clearly identified. The magnitude of each mode can be quantified by its height above the reference plane. The results of Figure A.1 reveal that the (3,2) mode has the highest modal effect for this configuration.

The control sources are placed in an array and grouped into control channels. Each control channel is then driven by a complex control input, U, described in Section 2. The modal influence factor due to all N_S control sources grouped into N_C control channels and driven by complex control inputs, U, can now be determined as

$$f_{m\mu}^{\alpha} = \{U\}^T \, [R] \, \{f_{m\mu}\} \tag{A.3}$$

where $\{U\}^T$ is the vector of N_C complex control inputs and the matrix $[R]$ is the control configuration matrix for the N_C control channels. Vector $\{f_{m\mu}\}$ is a $N_S x \, 1$ vector consisting of the modal influence factor, as described in Eq(A.2), for each of the N_S control sources.
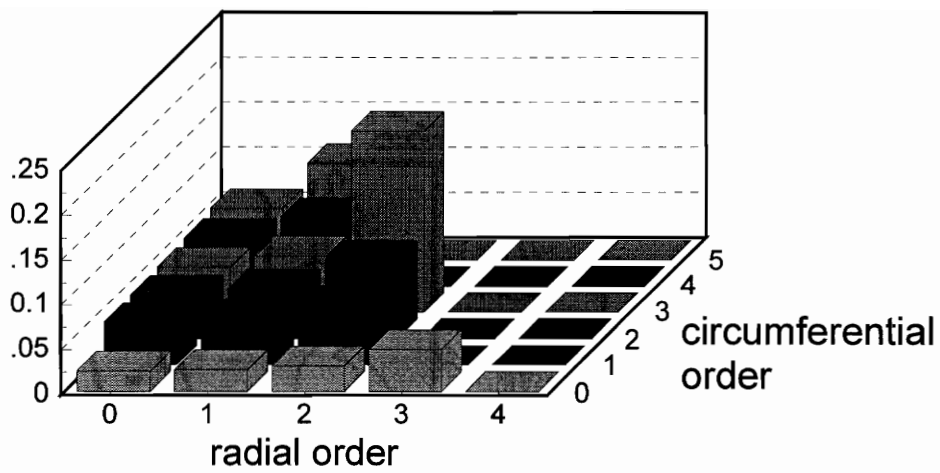
115

Figure A.1. Modal influence factor for a single point source.

To observe the superposition effect of the propagating modes on modal influence factor, the single control source array configuration of section 3.2 is employed. The control source array consists of twelve evenly distributed point sources, grouped into six control channels. Sources mounted on opposite sides of the duct are grouped into a control channel and driven with a phase difference of 180°. The complex control inputs used for this analysis are based on a control system with six far field error sensors as described in section 3.2. The complex control inputs are presented in Figure 3.7.

Figure A.2 presents the results of the modal superposition investigation. It is clear that only the first order spinning modes exist due to the combination of all control sources in the chosen configuration. In other words, the physical configuration of the control sources, combined with symmetric complex control inputs (equal magnitude), excites only the first order spinning modes.
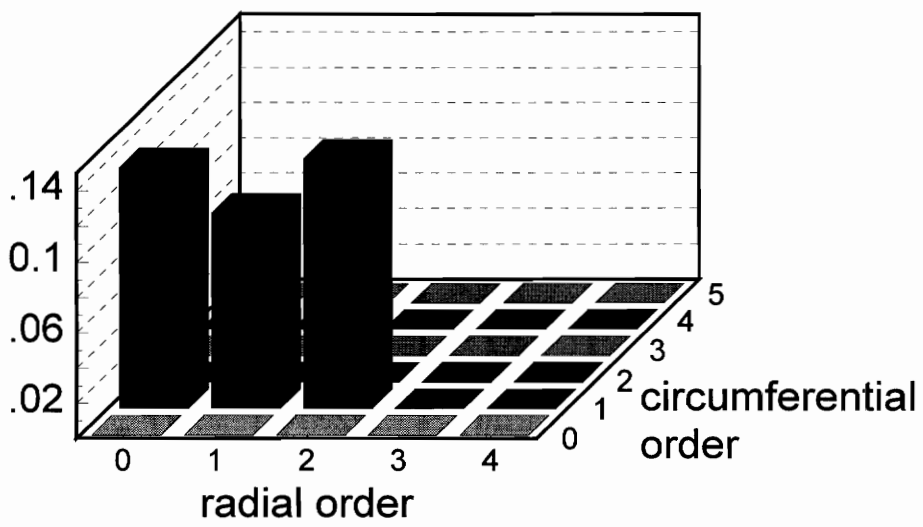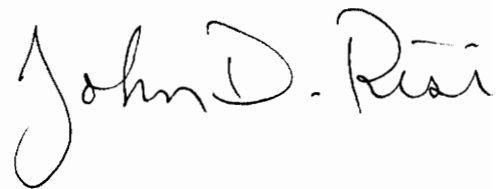
Figure A.2. Modal influence factor for an array of twelve control sources driven by symmetric complex control inputs.

Vita

John D. Risi was born in Pueblo, Colorado on October 7, 1964. Following graduation from Centennial High School in May 1983, John worked as a refrigeration service mechanic for Pepsi-Cola Bottling Group. He entered Colorado State University, located in Fort Collins, in the Fall of 1986. John received a Bachelor's Degree in Mechanical Engineering in the Spring of 1990. Upon graduation, he accepted a position in the product development group of Laser Magnetic Storage International in Colorado Springs. While employed at LMS, John played an integral part in the development of a third-generation tray-loading CD-ROM drive for the personal computer market. In February 1992, he accepted a temporary consulting position with the advanced development group of Exabyte Corporation in Boulder, Colorado. In August 1992, following their wedding, John and his wife moved to Blacksburg, Virginia for John to pursue his Master's Degree. In May 1994, John accepted a position with the Industrial Energy Center of Virginia Tech where he is currently employed as General Manager.